NASA/TM-2004-213273

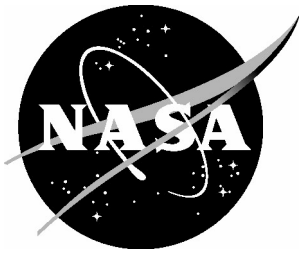

Computation of a Synthetic Jet in a Turbulent Cross-Flow Boundary Layer

Christopher L. Rumsey
Langley Research Center, Hampton, Virginia

October 2004

The NASA STI Program Office . . . in Profile

Since its founding, NASA has been dedicated to the advancement of aeronautics and space science. The NASA Scientific and Technical Information (STI) Program Office plays a key part in helping NASA maintain this important role.

The NASA STI Program Office is operated by Langley Research Center, the lead center for NASA's scientific and technical information. The NASA STI Program Office provides access to the NASA STI Database, the largest collection of aeronautical and space science STI in the world. The Program Office is also NASA's institutional mechanism for disseminating the results of its research and development activities. These results are published by NASA in the NASA STI Report Series, which includes the following report types:

- TECHNICAL PUBLICATION. Reports of completed research or a major significant phase of research that present the results of NASA programs and include extensive data or theoretical analysis. Includes compilations of significant scientific and technical data and information deemed to be of continuing reference value. NASA counterpart of peer-reviewed formal professional papers, but having less stringent limitations on manuscript length and extent of graphic presentations.

- TECHNICAL MEMORANDUM. Scientific and technical findings that are preliminary or of specialized interest, e.g., quick release reports, working papers, and bibliographies that contain minimal annotation. Does not contain extensive analysis.

- CONTRACTOR REPORT. Scientific and technical findings by NASA-sponsored contractors and grantees.

- CONFERENCE PUBLICATION. Collected papers from scientific and technical conferences, symposia, seminars, or other meetings sponsored or co-sponsored by NASA.

- SPECIAL PUBLICATION. Scientific, technical, or historical information from NASA programs, projects, and missions, often concerned with subjects having substantial public interest.

- TECHNICAL TRANSLATION. English-language translations of foreign scientific and technical material pertinent to NASA's mission.

Specialized services that complement the STI Program Office's diverse offerings include creating custom thesauri, building customized databases, organizing and publishing research results ... even providing videos.

For more information about the NASA STI Program Office, see the following:

- Access the NASA STI Program Home Page at ***http://www.sti.nasa.gov***

- E-mail your question via the Internet to help@sti.nasa.gov

- Fax your question to the NASA STI Help Desk at (301) 621-0134

- Phone the NASA STI Help Desk at (301) 621-0390

- Write to:
  NASA STI Help Desk
  NASA Center for AeroSpace Information
  7121 Standard Drive
  Hanover, MD 21076-1320

NASA/TM-2004-213273

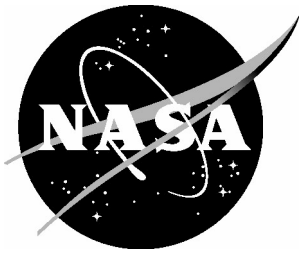

Computation of a Synthetic Jet in a Turbulent Cross-Flow Boundary Layer

Christopher L. Rumsey
Langley Research Center, Hampton, Virginia

National Aeronautics and
Space Administration

Langley Research Center
Hampton, Virginia 23681-2199

October 2004

Available from:

NASA Center for AeroSpace Information (CASI)
7121 Standard Drive
Hanover, MD 21076-1320
(301) 621-0390

National Technical Information Service (NTIS)
5285 Port Royal Road
Springfield, VA 22161-2171
(703) 605-6000

Contents

ABSTRACT

A series of unsteady Reynolds-averaged Navier-Stokes computations are performed for the flow of a synthetic jet issuing into a turbulent boundary layer through a circular orifice. This is one of the validation test cases from a synthetic jet validation workshop held in March 2004. Several numerical parameters are investigated, and the effects of three different turbulence models are explored. Both long-time-averaged and time-dependent phase-averaged results are compared to experiment. On the whole, qualitative comparisons of the mean flow quantities are fairly good. There are many differences evident in the quantitative comparisons. The calculations do not exhibit a strong dependence on the type of turbulence model employed.

1 INTRODUCTION

A CFD validation workshop on synthetic jets and turbulent separation control (CFDVAL2004) [1] was held in March 2004 in Williamsburg, VA. The purpose of the workshop was to assess the current capabilities of different classes of turbulent flow solution methodologies to predict flow fields induced by synthetic jets and separation control. Case 2 of the workshop was a synthetic jet issuing into a turbulent boundary layer through a circular orifice in the floor [2]. The flow was characterized by a forcing frequency of 150 Hz, with a maximum discharge vertical velocity of approximately $1.3U_\infty$.

The problem of synthetic jet flow in a turbulent boundary layer has been studied both experimentally (see, for example [3, 4, 5, 6]) and computationally (see, for example [7, 8, 9]). In general, this type of flow control may be useful for reducing separation or for achieving virtual aeroshaping. However, for the present investigation, the main purpose was an examination of the capability of CFD to accurately predict the unsteady flow physics of the particular experiment conducted for the workshop. This paper reports the results obtained using the unsteady Reynolds-averaged Navier-Stokes (URANS) equations computed with the code CFL3D [10]. Several other participants also computed this test case for the workshop; their results are summarized in Rumsey et al.[11], as well as on the CFDVAL2004 website.

The next section describes the CFL3D computer code. Then, the specifics of the test case are given, and the grid and boundary conditions are described. In the final two sections, the results are given, and conclusions are drawn.

2 NUMERICAL METHOD

The computer code CFL3D [10] solves the three-dimensional, time-dependent, Reynolds averaged compressible Navier-Stokes equations with an upwind finite-volume formulation (it can also be exercised in two-dimensional mode of operation for 2-D cases). It can solve flows over multiple-zone grids that are connected in a one-to-one, patched, or overset manner, and can employ grid sequencing, multigrid, and local time stepping when accelerating convergence to steady state. Upwind-biased spatial differencing is used for the inviscid terms, and flux limiting is used to obtain smooth solutions in the vicinity of shock waves, when present. Viscous terms are centrally differenced, and cross-diffusion terms are neglected. For very low Mach number flows, preconditioning [12] is used to insure convergence and accuracy of the solutions.

The CFL3D code is advanced in time with an implicit approximate factorization method. The implicit derivatives are written as spatially first-order accurate, which results in block tridiagonal inversions for each sweep. However, for solutions that utilize Roe flux-difference splitting [13], the block tridiagonal inversions are further simplified using a diagonal algorithm with a spectral radius scaling of the viscous terms.

In time-accurate mode, CFL3D uses pseudo-time stepping with multigrid and achieves second order temporal accuracy. With pseudo-time stepping, subiterations are used to reduce the linearization and factorization errors, and advance the solution in pseudo-time to the next physical time. For a non-deforming mesh, the time dependent compressible Navier-Stokes equations can be written as

$$\frac{1}{J}\frac{\partial \mathbf{Q}}{\partial t} = R(\mathbf{Q}) \tag{1}$$

where $\mathbf{Q}$ is the vector of conserved variables, J is the Jacobian of the generalized coordinate transformation, and R is the right-hand-side:

$$R(\mathbf{Q}) = -\left[\frac{\partial(\hat{\mathbf{F}} - \hat{\mathbf{F}}_v)}{\partial\xi} + \frac{\partial(\hat{\mathbf{G}} - \hat{\mathbf{G}}_v)}{\partial\eta} + \frac{\partial(\hat{\mathbf{H}} - \hat{\mathbf{H}}_v)}{\partial\zeta}\right] \tag{2}$$

made up of gradients of the inviscid and viscous flux terms. Eq. (1) can be discretized with backward differencing:

$$\frac{(1+\phi)(\mathbf{Q}^{n+1} - \mathbf{Q}^n) - \phi(\mathbf{Q}^n - \mathbf{Q}^{n-1})}{J\Delta t} = R(\mathbf{Q}^{n+1}) \tag{3}$$

The superscripts n, $n+1$, and $n-1$ indicate the time level. When $\phi = 0$ the method is first-order temporally accurate, and when $\phi = 1/2$ the method is second-order temporally accurate. To employ pseudo-time stepping, a pseudo time term (τ) is added to Eq. (3), and the equation is iterated in m, where m is the subiteration counter. After linearizing R and performing some additional manipulation, one obtains:

$$\begin{aligned}&\left[\left(\frac{1+\phi'}{J\Delta\tau} + \frac{1+\phi}{J\Delta t}\right)\mathbf{I} + \partial_\xi\mathbf{A} + \partial_\eta\mathbf{B} + \partial_\zeta\mathbf{C}\right]\Delta\mathbf{Q}^m = \\ &\frac{\phi'\Delta\mathbf{Q}^{m-1}}{J\Delta\tau} + \frac{\phi\Delta\mathbf{Q}^{n-1}}{J\Delta t} - \frac{(1+\phi)(\mathbf{Q}^m - \mathbf{Q}^n)}{J\Delta t} + R(\mathbf{Q}^m)\end{aligned} \tag{4}$$

where $\Delta\mathbf{Q}^m = \mathbf{Q}^{m+1} - \mathbf{Q}^m$, and

$$\mathbf{A} = \frac{\partial(\hat{\mathbf{F}} - \hat{\mathbf{F}}_v)}{\partial\mathbf{Q}} \qquad \mathbf{B} = \frac{\partial(\hat{\mathbf{G}} - \hat{\mathbf{G}}_v)}{\partial\mathbf{Q}} \qquad \mathbf{C} = \frac{\partial(\hat{\mathbf{H}} - \hat{\mathbf{H}}_v)}{\partial\mathbf{Q}} \tag{5}$$

Eq. (4) is approximately factored and written in primitive variable form; it is solved as a series of sweeps in each coordinate direction. Additional details are given in Krist et al.[10]. In the current study, several different physical time steps and number of subiterations were employed.

The turbulence models are solved uncoupled from the mean flow equations using implicit approximate factorization. Their advective terms are solved using first-order upwind differencing. Many turbulence models are available in CFL3D, but only those used in the current study are mentioned here. Descriptions of the one-equation Spalart-Allmaras (SA) and the two-equation Menter k-ω shear-stress transport (SST) turbulence models can be found in their respective references [14, 15]. Both of these models are linear eddy-viscosity models that make use of the Boussinesq eddy-viscosity hypothesis. The EASM-ko model is a nonlinear eddy-viscosity model in k-ω form. A detailed description of this model can be found in Rumsey and Gatski [16].

For time-accurate URANS computations, it can be shown that the dependent variables calculated correspond to phase-averaged variables [1]. In other words, when URANS is used, the computation eventually settles down to a repeatable periodic variation. Once this repeatability is attained, any point during the cycle corresponds to a phase-averaged result from the experiment. An example showing the cycle-to-cycle repeatability for a global integrated quantity is shown in Fig. 1. Here, coefficient of drag nondimensionalized by a unit reference length (the absolute level of which is not particularly meaningful in this case) is plotted as a function of iteration.

3 SPECIFICS OF THE TEST CASE

In this test case, flow passed in and out of a circular orifice 6.35 mm in diameter. The orifice was located on the floor of a wind tunnel splitter plate with a turbulent boundary layer at M=0.1 and approximate boundary layer thickness of 21 mm. The Reynolds number was 2230 per mm, or 14,160 per orifice diameter. The jet was driven electro-mechanically by a bottom-mounted square-shaped rigid piston mounted on an elastic membrane inside the cavity chamber beneath the splitter plate. The cavity was approximately 1.7 mm deep on average while the piston was operating, and the piston moved approximately ± 0.77 mm. The frequency was 150 Hz, and the maximum velocity out of the orifice was approximately $1.3U_\infty$.

A schematic diagram showing the cavity and diaphragm is shown in Fig. 2. Because the cavity was so shallow, its volume changed dramatically during the course of one cycle of motion, from (very roughly) 10,000 mm^3 to 26,000 mm^3. Also, it should be noted that the solid plate was affixed to the flexible membrane in such a way that the geometry of the piston face was not perfectly symmetric about the centerplane. This misalignment possibly could have been a cause of asymmetries noted in the experimental data, as described in the next section.

4 DESCRIPTION OF GRID AND BOUNDARY CONDITIONS

For the computations, the fine grid was a 7-zone structured grid with 4.1 million grid points (3.9 million cells). It is shown in Fig. 3. It was created specifically for use in the CFDVAL2004 workshop, and was posted to the workshop's website. The grid was in units of millimeters, and its 7 zones were connected in a 1-to-1 fashion. This grid system extended 0.0508 m upstream of center of the orifice, and 0.1016 m downstream of the center of the orifice. Its height was 0.076 m above the floor, and its width extended from y=-0.038 m to +0.038 m (total width of 0.076 m). Note that this height and width were smaller than the wind tunnel height (approx 0.249 m) and width (0.381 m).

At the tunnel floor, the viscous normal wall spacing was set to 0.002 mm. On the wall of the circular orifice near where the jet exits, the spacing was 0.0025 mm. As this orifice wall extended into the cavity and curved around (forming the upper wall of the cavity), its normal grid spacing relaxed to approximately 0.02 mm. The other walls inside the cavity (including the lower wall) had inviscid-type wall grid spacing. A medium level grid was created by removing every other point from the fine grid; the resulting grid had 0.53 million grid points (0.49 million cells).

The coordinate system was the same in the experiment and computations: x ran downstream, y spanwise, and z up. The origin ($x = 0$, $y = 0$, $z = 0$) was located 50.8 mm upstream of the center of the orifice at the center plane on the splitter plate floor. Thus, the orifice front edge was at $x = 47.625$ mm and its back edge was at $x = 53.975$ mm.

Fig. 4 shows a center plane cut through the medium level grid (near the orifice), along with notes describing the boundary conditions applied. The bottom wall of the tunnel, the wall of the hole itself, and the top wall of the cavity were all specified as viscous, adiabatic walls. The four side walls of the cavity were taken to be inviscid walls. The outside farfield boundaries on the top, sides, and outflow were all solved using a farfield Riemann invariant boundary condition. At the inflow, the velocity and turbulence boundary values were set to approximate a fully-developed turbulent boundary layer with boundary layer thickness of approximately 21

mm; the density was set to freestream level and the pressure was extrapolated from the interior of the domain. The u-velocity profile and $u'w'$ turbulent shear stress profile are shown in Figs. 5 and 6. The specified approximate profiles are in fairly good agreement with the experimental data.

Finally, on the bottom wall of the cavity, a time-dependent velocity was prescribed:

$$u = 0 \qquad v = 0 \qquad w = [(\rho w)_{\max}/\rho] cos(2\pi F t) \tag{6}$$

where F is the frequency and t is the time. With this boundary condition, the density and pressure were extrapolated from the interior of the domain. The $(\rho w)_{\max}$ was chosen in order to achieve an approximate match of the vertical velocity component at the outflow of the orifice with the experiment (the final value used was $(\rho w)_{\max} = 0.0008 \rho_\infty a_\infty$, where a_∞ is the reference speed of sound). The resulting w and u components of velocity at the orifice exit can be seen in Figs. 7 and 8. In general, the computation captured the vertical velocity maximum and minimum levels, but failed to capture the sharp peak in w and the additional hump on the downstroke. The streamwise velocity component agreed fairly well with experiment, except that the maximum near phase of 320° was underpredicted.

It should be noted that the experimental data exhibited significant side (v-component) velocities during the cycle at this location, whose cause has not been accounted for. See Fig. 9. The current CFD method made no attempt to duplicate this v-velocity component. (In the computations, v along the centerplane was approximately zero, because the grid was symmetric about the centerplane and there was nothing other than numerical discretization error to drive any asymmetries in the solution.) As discussed in Section 3, the cavity was very shallow, and its volume changed by more than a factor of two during its motion. It is possible that inherent asymmetries in the piston device may have been a contributing factor in the large v-component of velocity at the orifice exit. It is also possible that the experimental data was taken slightly off-center-plane. However, the CFD v-velocities off-center-plane were fairly small in magnitude. See, for example, Fig. 10, which shows computed v-velocities in the plane $z = 0.4$ mm above the orifice at phase = 160°. In this plot, the red lines denote zone boundaries in the grid; the outer circle represents the outer edge of the orifice. The maximum magnitude of v-velocity within 1 mm of the orifice center was less than $0.13 U_\infty$.

5 RESULTS

Fig. 11 shows the locations where most of the comparisons were made with experimental data, obtained via three-component laser doppler velocimetry (LDV). Particle image velocimetry (PIV) data were also taken in the experiment, but these are only used to compare velocity contours in two planes downstream of the orifice. The computations are summarized in Table 1. The nomenclature gives first the model used, followed by the number of steps per cycle, then number of subiterations. The letter "f" at the end refers to fine grid, whereas "m" refers to medium grid. For example, "SA-720-10m" stands for the SA model with 720 steps per cycle and 10 subiterations on the medium grid.

Only the SA model was run on both the fine and medium grids; the other turbulence models were run on the medium grid alone. The SA model was run with 720 steps per cycle (nondimensional time step of $\Delta t = 3.203704$) and a range of subiterations from 5 to 20. The SST model was run with both 720 steps per cycle with 5 subiterations and 10 subiterations, as

Table 1: Summary of nomenclature associated with computations performed

Time advancement method	SA (fine)	SA (med)	SST (med)	EASM-ko (med)
720 steps/cycle, 5 subits	SA-720-5f	SA-720-5m	SST-720-5m	
720 steps/cycle, 10 subits		SA-720-10m	SST-720-10m	
720 steps/cycle, 20 subits		SA-720-20m		
1440 steps/cycle, 10 subits			SST-1440-10m	EASM-1440-10m

well as 1440 steps per cycle (nondimensional time step of $\Delta t = 1.601852$) with 10 subiterations. The EASM-ko model was run with 1440 steps per cycle and 10 subiterations.

Figs. 12, 13, and 14 show the effects of number of subiterations on the time history of velocity at three points in the flow: 0.4 mm above the orifice (just upstream of its center), 1D downstream of the orifice center and 10 mm above the wall, and 2D downstream of the orifice center and 10 mm above the wall. At all locations there was a relatively small effect between 5 and 10 subiterations, and almost no effect between 10 and 20 subiterations. Plots of the log of the L_2-norm of the density and turbulence model equation residuals as a function of subiterations is shown in Figs. 15, 16, and 17 for 5, 10, and 20 subiterations, respectively. For 5 subiterations, the L_2-norm of the density residual drops almost 1 order of magnitude (at this point in the cycle). For 10 subiterations, it drops almost 1.5 orders, and for 20 subiterations, it drops between 1.5 and 2 orders. The L_2-norm of the turbulence quantity residual drops almost 2 orders for 5 subiterations, slightly more than 2 orders for 10 subiterations, and about 2.5 orders for 20 subiterations.

The computations were performed for the most part on a dual processor Intel Xeon 2.4 GHz PC with 2 gigabytes of DDR ECC memory. The solution ran in approximately 11 seconds per subiteration on the medium grid for SA and SST, and approximately 14 seconds per subiteration on the medium grid for EASM-ko. For example, using SA and 10 subiterations per time step, the solution on the medium grid ran in approximately 22 hours for 1 cycle (720 time steps, or 7200 total subiterations). At least 4 – 5 cycles were needed to establish a repeatable cyclical solution.

For the SST model, an instability was noted in the solution when 5 subiterations were employed with 720 steps per cycle. This instability showed up as a series of un-physical oscillations in the flowfield variables at given points in space during part of the cycle. By increasing the number of subiterations and halving the time step, the magnitude of the instability was dramatically reduced. Fig. 18 shows the effect of these variations on the time-dependent behavior of a point in the flow where the oscillations were evident. Other than at this point in the flow (1D downstream of the orifice center), there was very little effect evident when varying the time step from 720 to 1440 steps per cycle for the SST model. For example, time histories are shown at the location 2D downstream using SST in Fig. 19. The results using 5 subiterations still showed some oscillatory behavior, but results using two different time steps with 10 subiterations were nearly identical. No oscillations were evident for the SA or EASM-ko models, although the EASM-ko model would not run with 720 steps per cycle.

Results are now presented for several quantities in comparison with experimental data. In all of the plots, the following results are shown: SA-720-5f, SA-720-5m, SST-1440-10m, and EASM-1440-10m. The fine grid computation using SA was only run using 5 subiterations. Although earlier results showed that at least 10 subiterations were required to achieve solutions that were almost completely independent of the number of subiterations, the use of 5 subiterations showed

only minor differences. Therefore, the results using 5 subiterations with SA are still expected to be very close to the fully-temporally-converged solution. (SA results on the medium grid are also shown with 5 subiterations so that a direct comparison can be made of the effect of grid alone.)

Time histories at three points in the field are shown in Figs. 20, 21, and 22. There are differences in the computations both due to grid size and turbulence model, but for the most part these differences are small in comparison to the differences between CFD and experimental data. With the exception of missing a few of the peak levels, the CFD results capture the overall trends in the experimental data fairly well. (Differences between CFD and experimental data just above the orifice in Fig. 20 were discussed earlier in Section 4.)

Long-time-average velocity profiles at various x-locations along the centerplane are given in Figs. 23 – 28. There were only minor differences due to grid or turbulence model for these results, and agreement with experimental data was very good overall. The largest differences with experimental data occurred at the station 1D downstream. There, the u-velocity was predicted slightly too large in the inner part of the boundary layer, and the w-component showed larger differences but a similar structure (double peak) as experimental data.

Long-time-average velocity profiles at two z-locations above the wall in the centerplane are given in Figs. 29 and 30. Along $z = 0.4$ mm, there was good agreement with the limited u-velocity experimental data, but agreement with w-velocity data was not as good. Along $z = 10$ mm, both velocity components were in reasonably good agreement with the data. The largest variation among the CFD results occurred for the w-velocity component at the downstream end of the $z = 10$ mm line, with the fine grid results in best agreement with the data.

Phase-averaged velocity comparisons are made in Figs. 31 – 39 for 1D upstream. Results were in very good agreement with experimental data at all phases except phase = 240°. Here, it appears that the CFD computation had "gotten ahead of" the experiment. In other words, the computation was well into in the suction phase, whereas the experiment was not. This can be clearly seen by referring back to Fig. 20: at phase = 240°, the CFD had a large negative vertical velocity component over the orifice, whereas the experimental data showed a near zero vertical velocity component (heading negative).

Phase-averaged velocity comparisons are made in Figs. 40 – 48 for 1D downstream. The results were in fair agreement with the data at this station, with the worst agreement again at phase = 240°. Also, at phase = 80°, the reverse-flow region in the computations extended higher, and there was an slight overshoot in velocity near z=6 mm. Results are also given for 8D downstream in Figs. 49 – 57. At this location, computations still agreed qualitatively very well with experimental data, but there were many quantitative differences. This far downstream, the CFD variation due to grid and turbulence models tended to be the larger than at the upstream locations.

Two of the turbulence quantities, $u'w'$ and $u'u'$, are shown at two stations and four phases in Figs. 58 – 65. The agreement with experimental data was sometimes good and sometimes poor. Overall there was greater CFD variation in the turbulence quantities than in the mean flow velocities. However, no one turbulence model stood out as being consistently superior.

The experiment also used PIV to acquire data in several planes for this case. Long-time-average contours of u-velocity, along with v-w velocity vectors, are shown in Figs. 66 and 67 at the plane 1D downstream. (Note that the v and w components of velocity from the PIV were not consistent with other measurement techniques, so they should be viewed qualitatively only.)

Here, results are only shown for SA on the fine grid; results on the medium grid and with different turbulence models were very similar. Both experimental data and CFD results indicated the presence of counter-rotating vortices. However, the computation exhibited a tighter and more strongly-defined structure, located higher from the wall than the experimental data. CFD results were also approximately symmetric about the centerplane, whereas the experimental data was not. Long-time-average results at the plane 4D downstream are shown in Figs. 68 and 69. At this location, the CFD results were in fairly good qualitative agreement with the experimental data. The vortex centers in the computation were near $z = 8$ mm, and the vortex centers in the experiment were between $z = 8$ – 10 mm. Again, the experimental data was not symmetric about the centerplane.

Phase-averaged contours of u-velocity are compared in Figs. 70 – 74 for phase = 120° at the plane 1D downstream, using SA on both the fine and medium grids, as well as SST and EASM-ko on the medium grid. Computed results agreed qualitatively with experimental data, and both grids and all turbulence models gave similar results. Additional comparisons are given in Figs. 75 – 84. In these figures, only SA results on the fine grid are shown (results on the medium grid and results using different turbulence models were very similar). At phase = 200°, the computation showed a larger, more concentrated structure 1D downstream than in the experiment. At phase = 280°, the results returned to being qualitatively similar. At the plane 4D downstream, the computation showed more of a perturbation (larger structure) than the experiment at phase = 120°, qualitatively similar results at phase = 200°, then less of a perturbation (smaller structure) than the experiment at phase = 280°.

At the center plane, phase-averaged contours of u-velocity are shown in the region over the orifice in Figs. 85 – 92. At phases of 40° and 120°, the experimental data and CFD results were qualitatively similar, whereas at phases of 200° and 280°, they were quite different. These latter two phases occurred during the downstroke (suction part) of the cycle.

It is also interesting to look at contours of the vertical (w-component) of velocity in the plane $z = 0.4$ mm above the orifice as a function of phase. Computed results are shown in Figs. 93 – 96 (there were no corresponding experimental results available for comparison). At phase = 40°, there was nearly uniform near-zero vertical velocity over the orifice. At phase = 120°, the expulsion velocity out of the orifice was near its peak and was very nonuniform, with the maximum (of approximately $2U_\infty$) located along the edge of the orifice between the sides and the downstream end. At phase = 200°, the contours were similarly nonuniform, but lower in magnitude. Finally, at phase = 280°, the flow was indicating suction into the orifice, with the peak suction located off-center, closer to the downstream end. The nonuniformities evident in these computational results highlight the importance of including the cavity in this type of computation (rather than imposing a top-hat or other simple sinusoidal boundary condition directly at the orifice boundary), in order to capture the near-field physics correctly.

6 CONCLUSIONS

A URANS CFD code was used to compute the unsteady flow of a synthetic jet issuing into a turbulent boundary layer through a circular orifice. The computation modeled the cavity and applied an assumed sinusoidal time-dependent boundary condition on the stationary grid at the piston location. This boundary condition enabled the computation to capture the minimum and maximum vertical velocities at the orifice exit, but several other aspects of the experimental data were missed. Although there were many differences evident in the quantitative

comparisons, CFD was successful overall at predicting many global flow features – including both long-time-averaged and phase-averaged velocities – compared to experiment. Turbulence quantities generally did not agree very well with experimental data. Numerical parameters were investigated, and showed that the grid, time step, and number of subiterations were sufficient to capture the essential features of this flow field. The calculations did not exhibit a strong dependence on the type of turbulence model employed.

ACKNOWLEDGMENTS

The author gratefully acknowledges N. W. Schaeffler, H. L. Atkins, and V. N. Vatsa of NASA Langley Research Center for their helpful discussions and feedback during the course of this project.

References

[1] Sellers, W. L. and Rumsey, C. L., "Langley Research Center Workshop: CFD Validation of Synthetic Jets and Turbulent Separation Control," http://cfdval2004.larc.nasa.gov, 2004.

[2] Schaeffler, N. W. and Jenkins, L. N., "The Isolated Synthetic Jet in Crossflow: A Benchmark for Flow Control Simulation," AIAA paper 2004-2219, June-July 2004.

[3] Gordon, M. and Soria, J., "PIV Measurements of a Zero-Net-Mass-Flux Jet in Cross Flow," *Exp. Fluids*, Vol. 33, 2002, pp. 863–872.

[4] Smith, D. R., "Interaction of a Synthetic Jet with a Crossflow Boundary Layer," *AIAA J.*, Vol. 40, No. 11, 2002, pp. 2277–2288.

[5] Zaman, K. B. M. Q. and Milanovic, I. M., "Synthetic Jets in Cross-Flow. Part I: Round Jet," AIAA paper 2003-3714, June 2003.

[6] Sauerwein, S. C. and Vakili, A. D., "An Experimental Study of Zero-Mass Jets in Crossflow," AIAA paper 99-0668, January 1999.

[7] Cui, J., Agarwal, R. K., and Cary, A. W., "Numerical Simulation of the Interaction of a Synthetic Jet with a Turbulent Boundary Layer," AIAA paper 2003-3458, June 2003.

[8] Mittal, R., Rampunggoon, P., and Udaykumar, H. S., "Interaction of a Synthetic Jet with a Flat Plate Boundary Layer," AIAA paper 2001-2773, June 2001.

[9] Mittal, R. and Rampunggoon, P., "On the Virtual Aeroshaping Effect of Synthetic Jets," *Phys. Fluids*, Vol. 14, No. 4, 2002, pp. 1533–1536.

[10] Krist, S. L., Biedron, R. T., and Rumsey, C. L., "CFL3D User's Manual (Version 5.0)," NASA TM-1998-208444, June 1998.

[11] Rumsey, C. L., Gatski, T. B., Sellers, W. L. III, Vatsa, V. N., and Viken, S. A., "Summary of the 2004 CFD Validation Workshop on Synthetic Jets and Turbulent Separation Control," AIAA paper 2004-2217, June-July 2004.

[12] Weiss, J. M., and Smith, W. A., "Preconditioning Applied to Variable and Constant Density Flows," *AIAA Journal*, Vol. 33, No. 11, 1995, pp. 2050–2057.

[13] Roe, P. L., "Approximate Riemann Solvers, Parameter Vectors, and Difference Schemes," *J. Computational Physics*, Vol. 43, 1981, pp. 357–372.

[14] Spalart, P. R., and Allmaras, S. R., "A One-Equation Turbulence Model for Aerodynamic Flows," *La Recherche Aerospatiale*, No. 1, 1994, pp. 5–21.

[15] Menter, F. R., "Two-Equation Eddy-Viscosity Turbulence Models for Engineering Applications," *AIAA Journal*, Vol. 32, No. 8, 1994, pp. 1598–1605.

[16] Rumsey, C. L. and Gatski, T. B., "Summary of EASM Turbulence Models in CFL3D with Validation Test Cases," NASA/TM-2003-212431, June 2003.

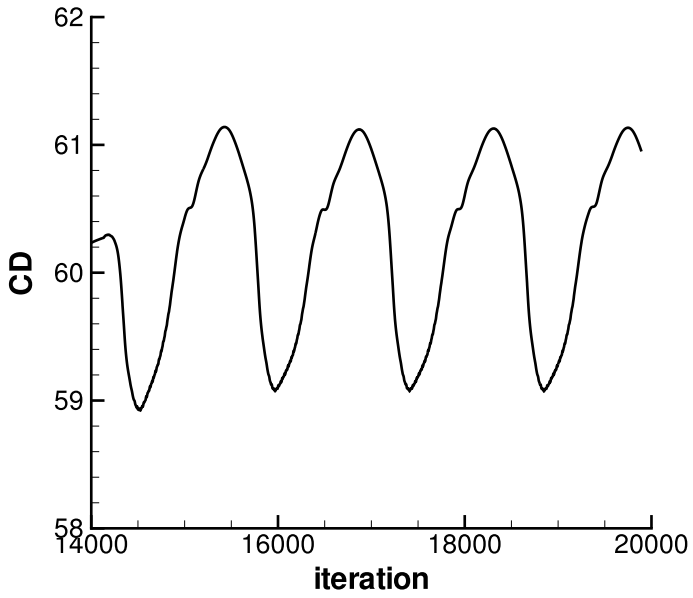

Figure 1: Sample drag coefficient as a function of iteration, showing periodic repeatability of URANS computation.

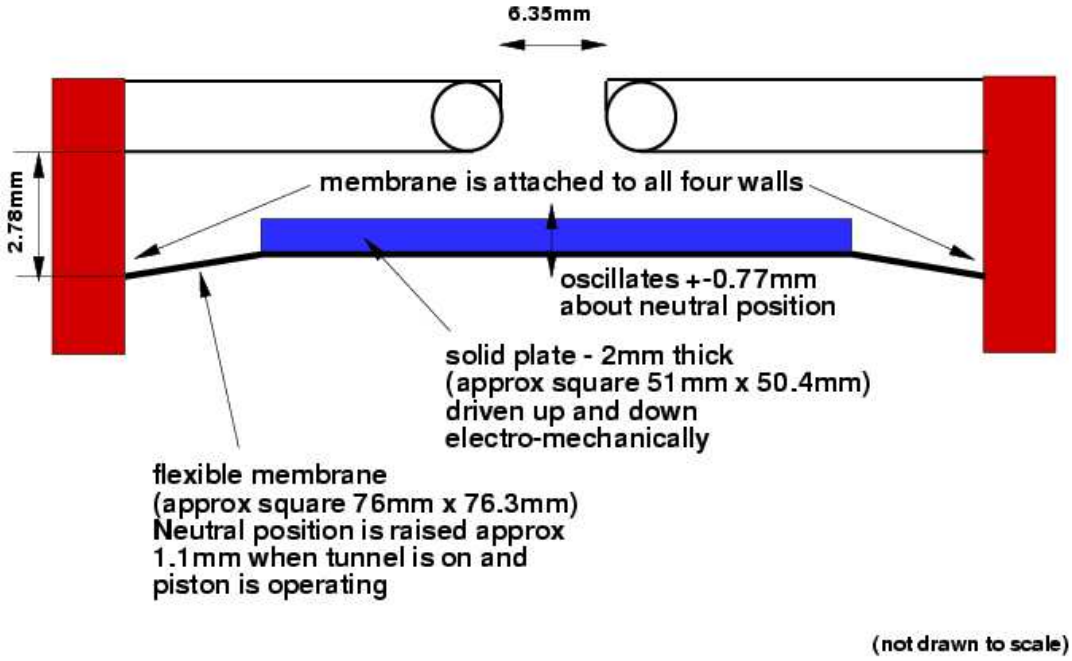

Figure 2: Sketch of cavity and diaphragm.

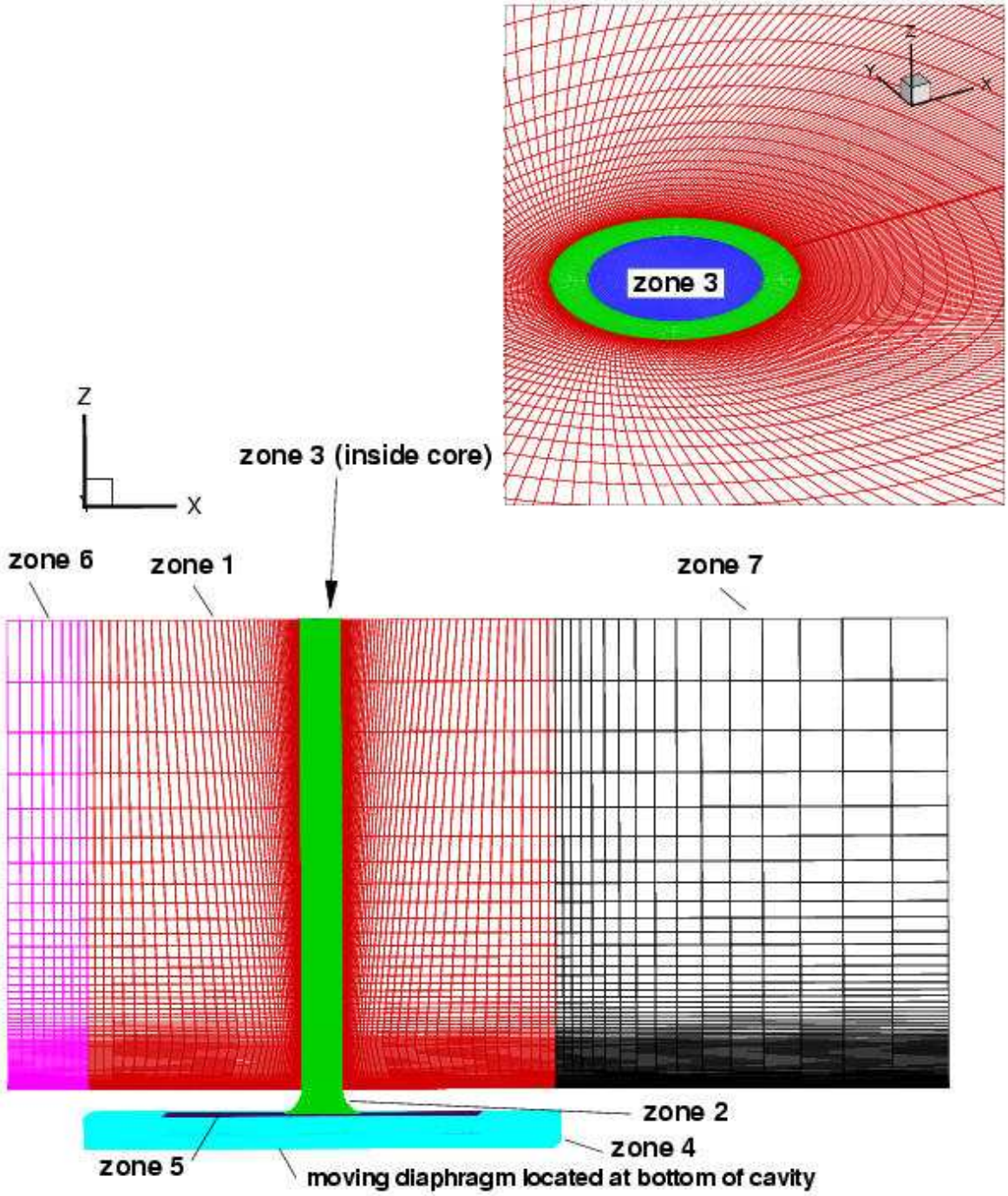

Figure 3: Sketch of 7-zone structured grid.

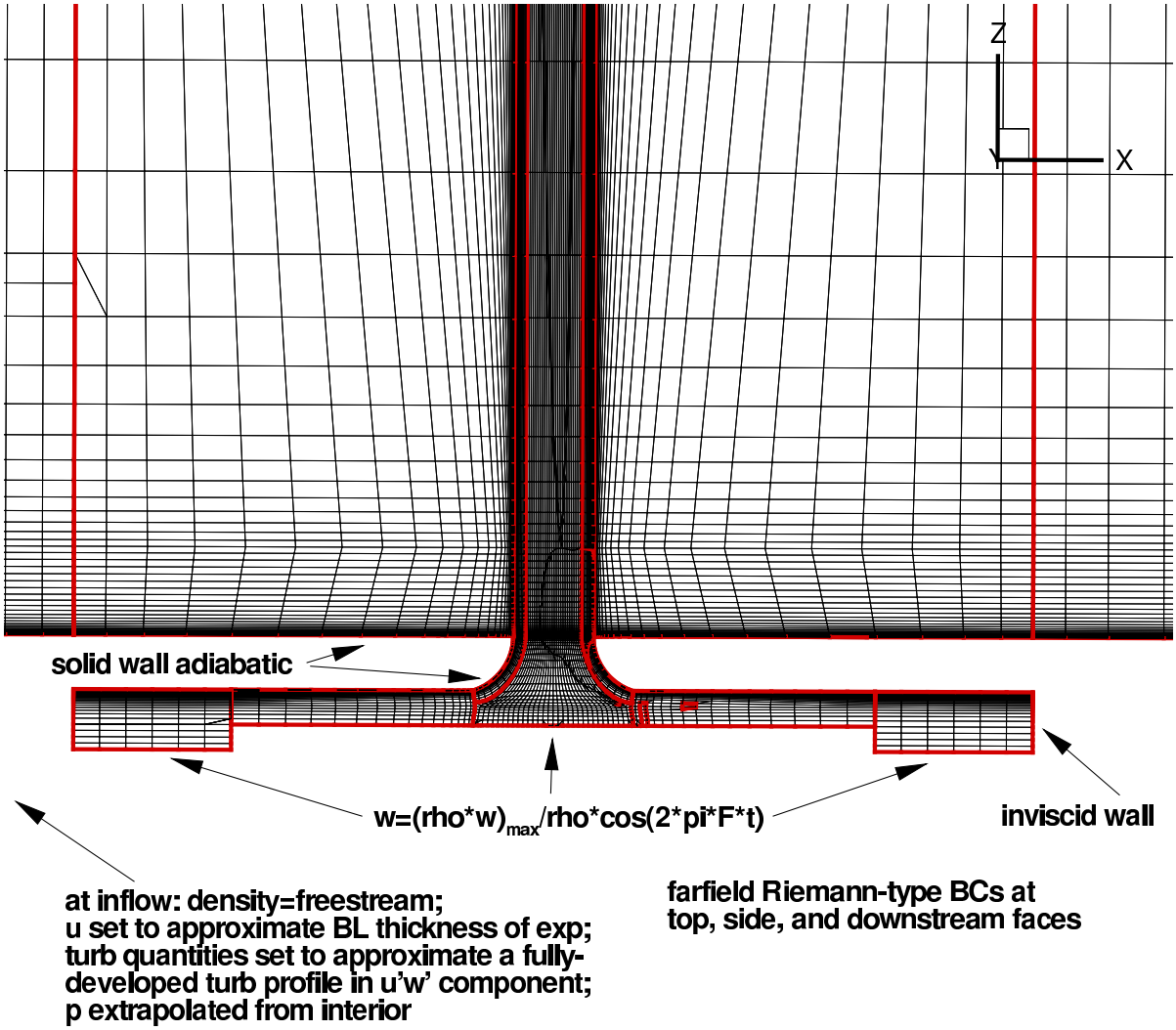

Figure 4: Cross-section of medium grid, with description of boundary conditions.

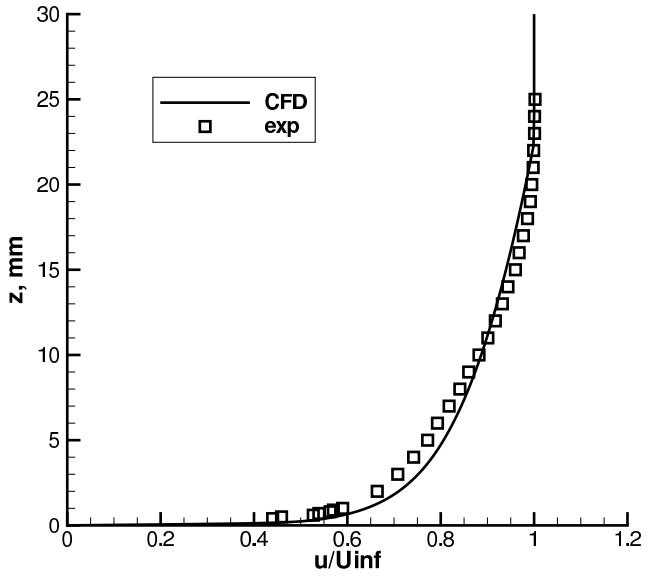

Figure 5: Streamwise velocity component at the inflow plane, $x = 0$ mm.

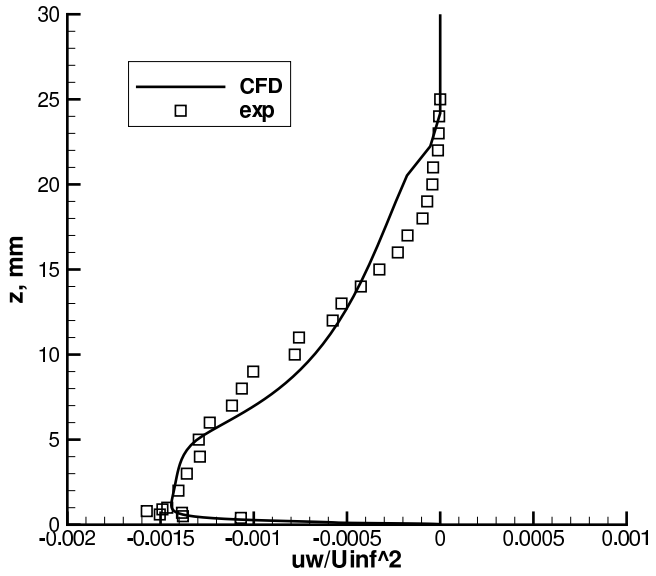

Figure 6: Turbulent shear stress ($u'w'$) at the inflow plane, $x = 0$ mm.

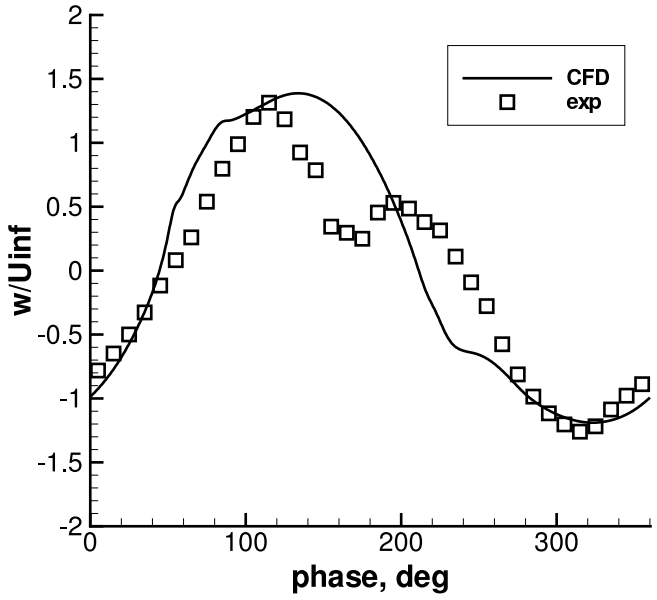

Figure 7: Vertical velocity component at the orifice exit.

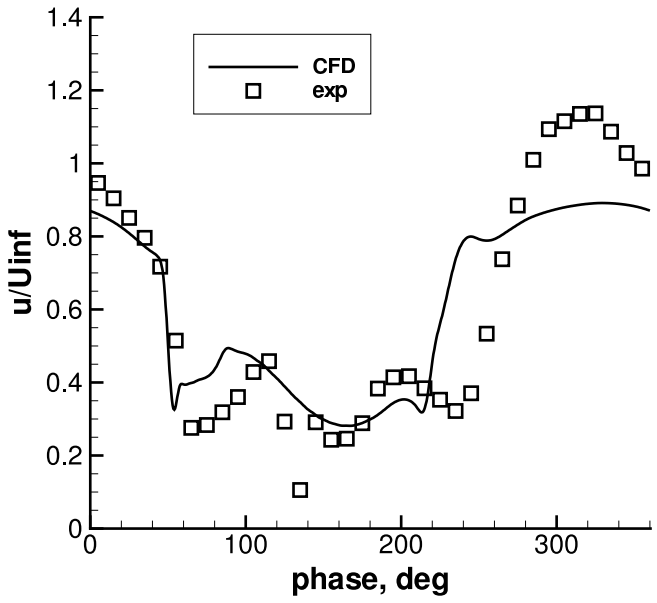

Figure 8: Streamwise velocity component at the orifice exit.

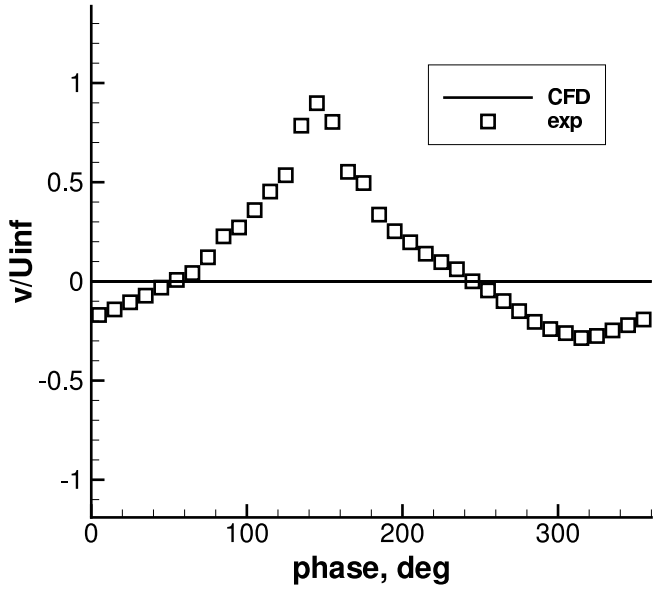

Figure 9: Spanwise velocity component at the orifice exit.

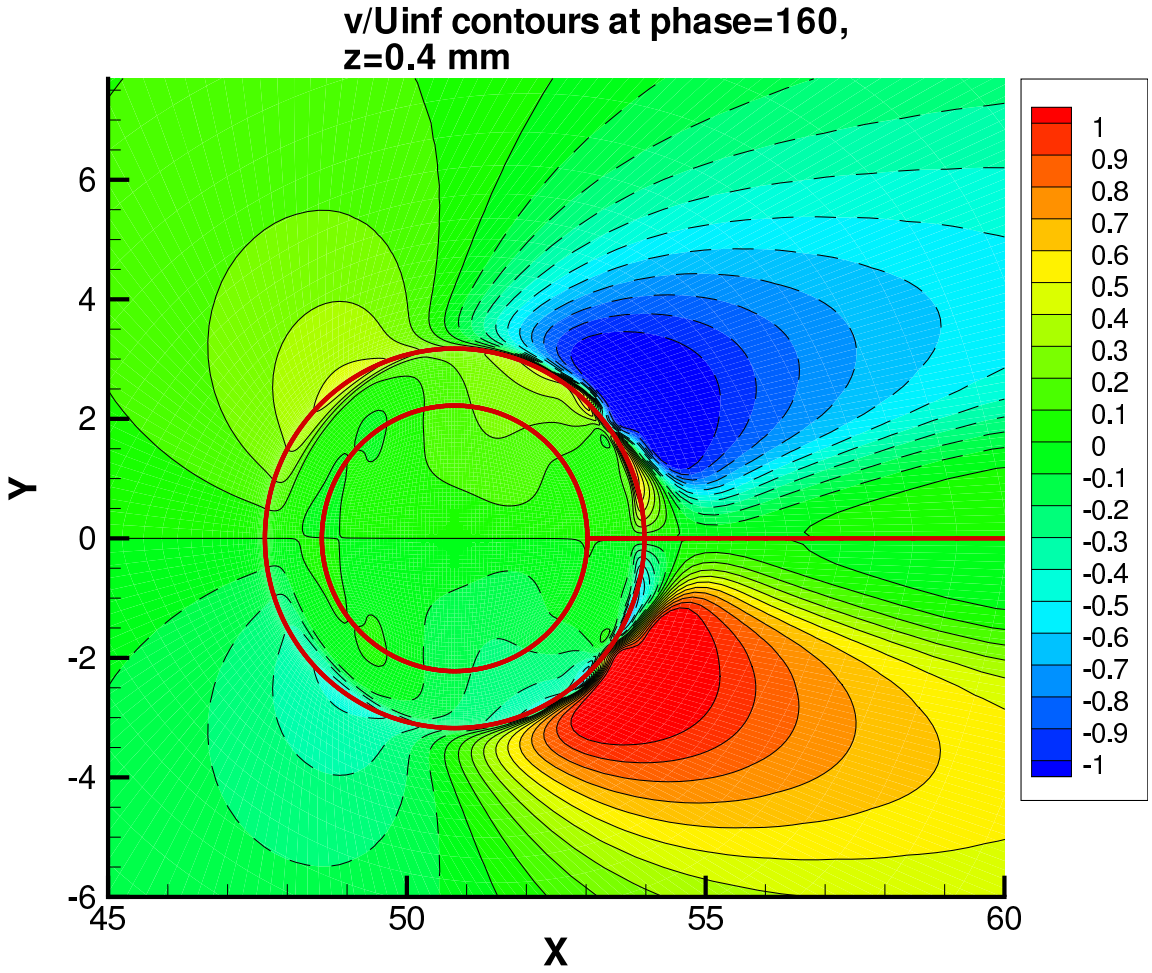

Figure 10: Contour plot of v-velocities at $z = 0.4$ mm above the orifice at phase = 160° (outer circle denotes orifice location).

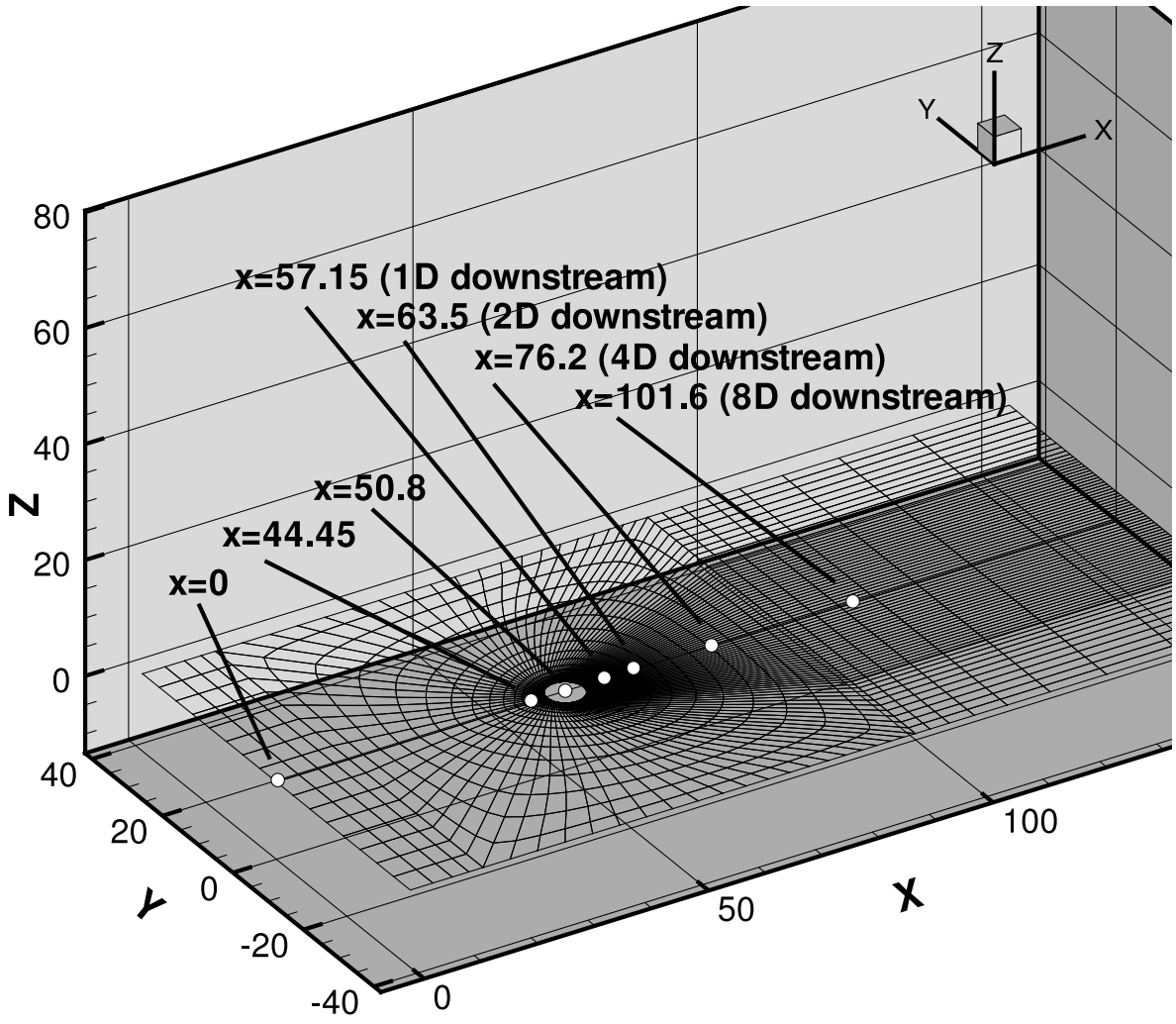

Figure 11: Sketch showing locations where data were compared with experiment.

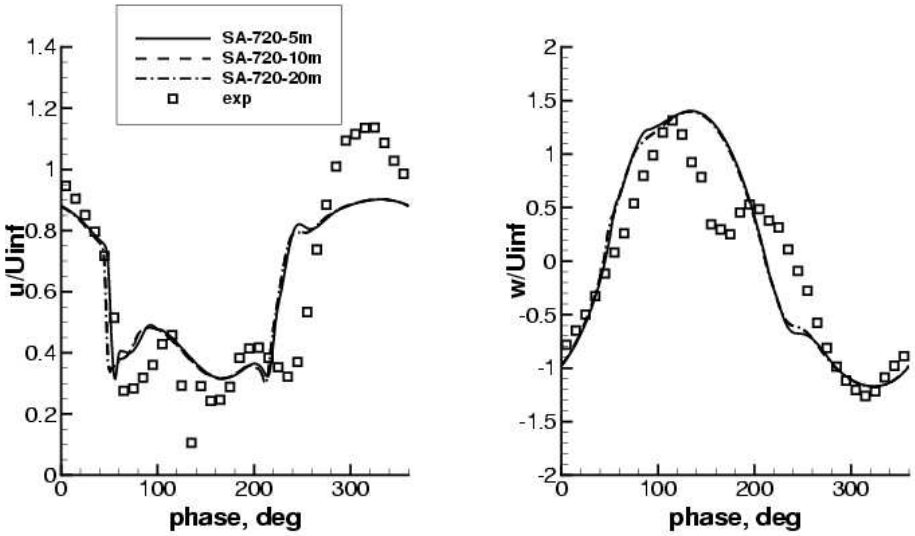

Figure 12: Effect of number of subiterations on velocity at $x = 50.63$ mm, $y = 0$, $z = 0.4$ mm (over the orifice), SA model on medium grid, 720 steps per cycle.

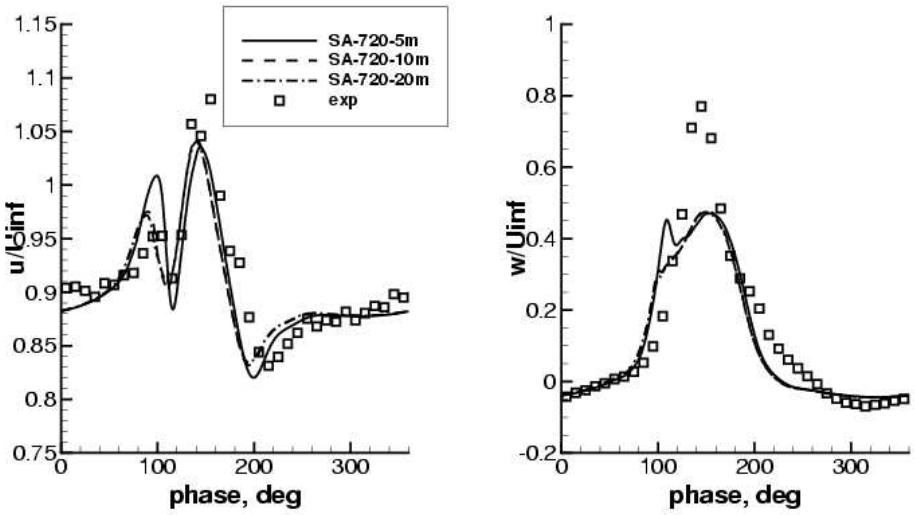

Figure 13: Effect of number of subiterations on velocity at $x = 57.15$ mm, $y = 0$, $z = 10$ mm (1D downstream), SA model on medium grid, 720 steps per cycle.

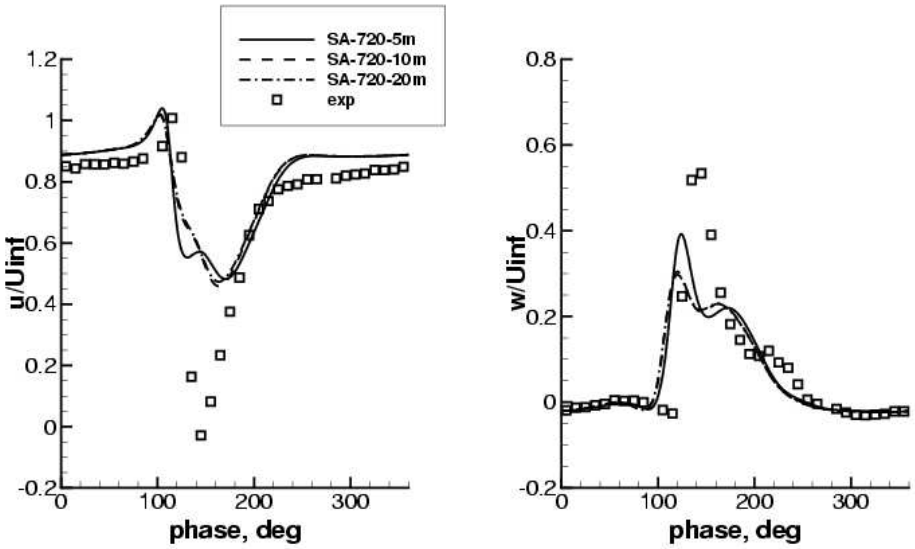

Figure 14: Effect of number of subiterations on velocity at $x = 63.5$ mm, $y = 0$, $z = 10$ mm (2D downstream), SA model on medium grid, 720 steps per cycle.

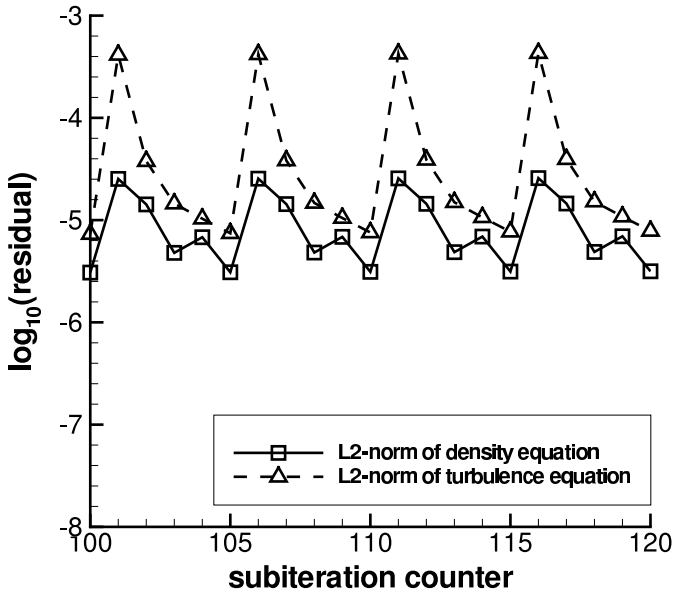

Figure 15: Residual history as a function of subiterations for SA model with 5 subiterations per time step.

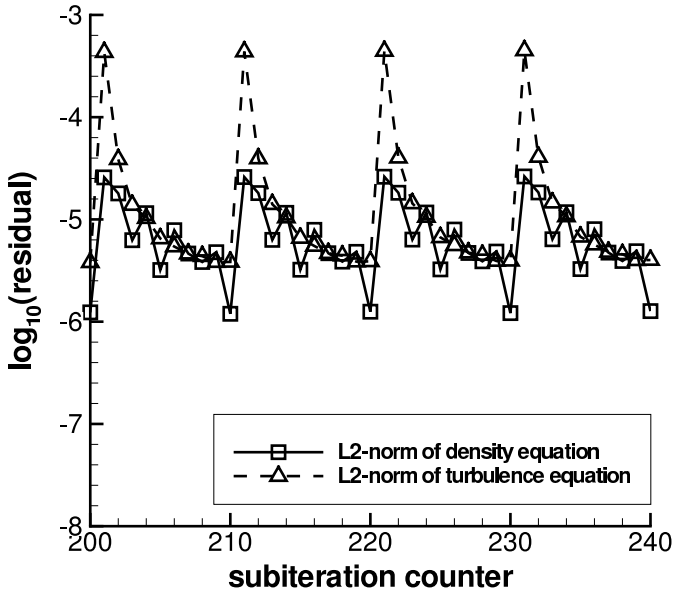

Figure 16: Residual history as a function of subiterations for SA model with 10 subiterations per time step.

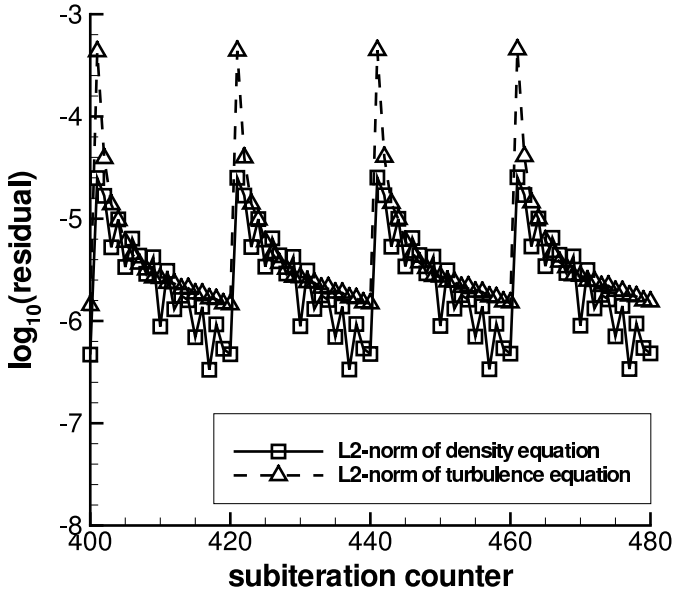

Figure 17: Residual history as a function of subiterations for SA model with 20 subiterations per time step.

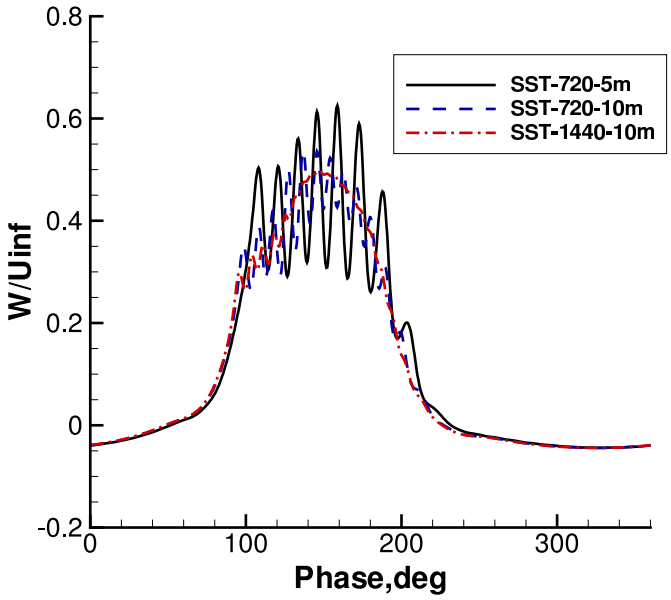

Figure 18: Effect of steps per cycle and number of subiterations on vertical velocity at $x = 57.15$ mm, $y = 0$, $z = 10$ mm (1D downstream), SST model on medium grid.

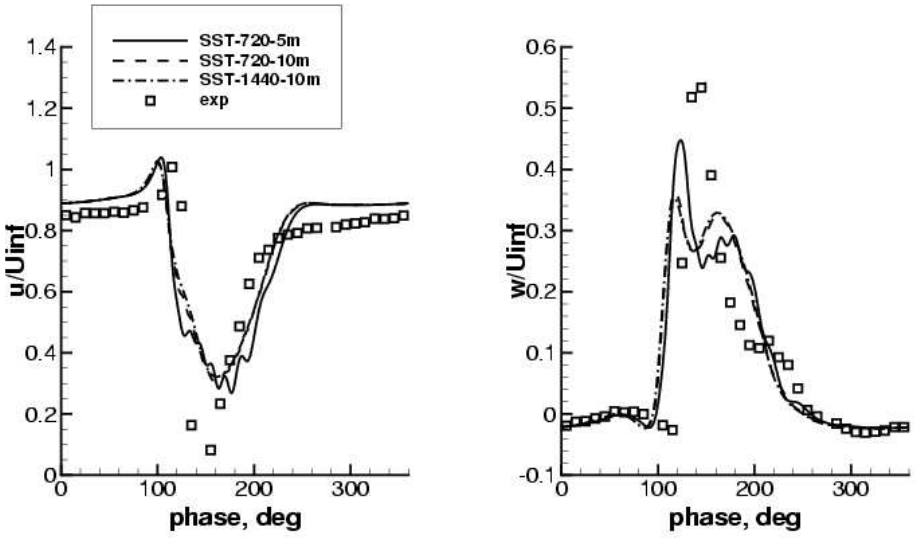

Figure 19: Effect of steps per cycle and number of subiterations at $x = 63.5$ mm, $y = 0$, $z = 10$ mm (2D downstream), SST model on medium grid, 10 subiterations.

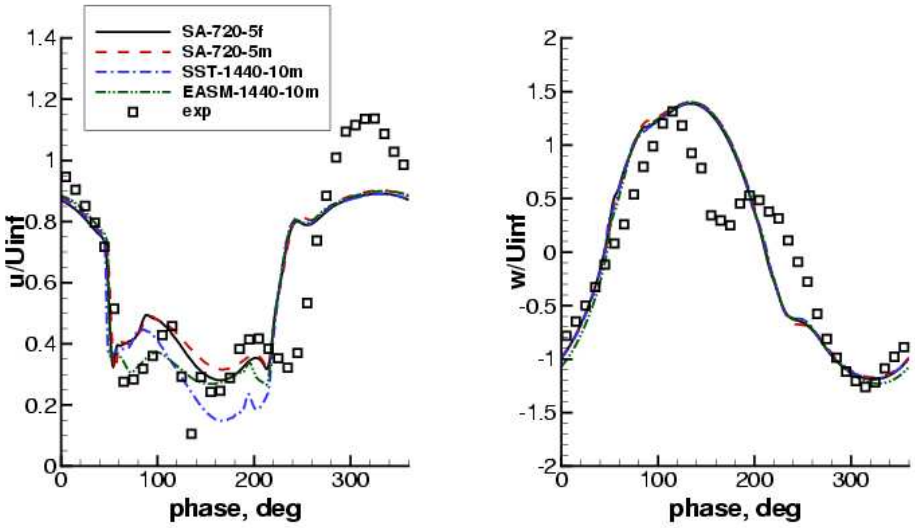

Figure 20: Time history at $x = 50.63$ mm, $y = 0$, $z = 0.4$ mm (over the orifice).

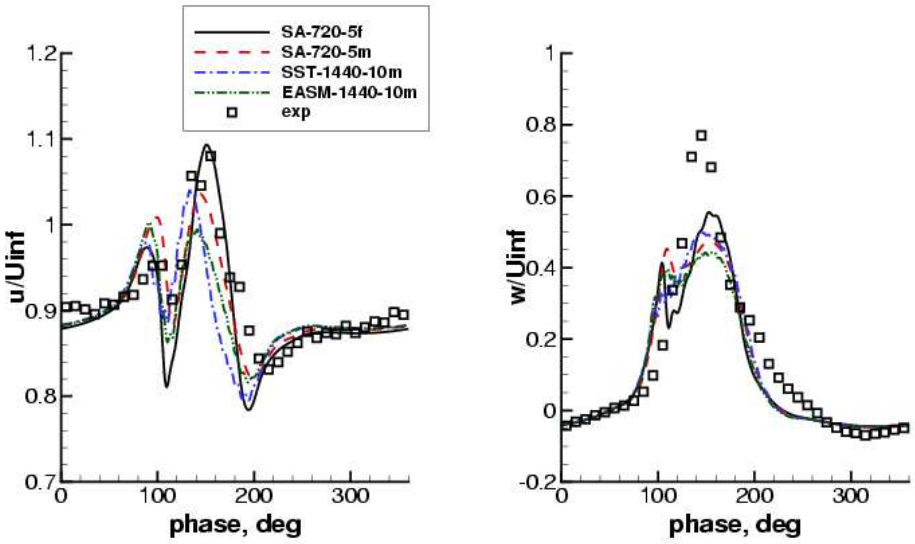

Figure 21: Time history at $x = 57.15$ mm, $y = 0$, $z = 10$ mm (1D downstream).

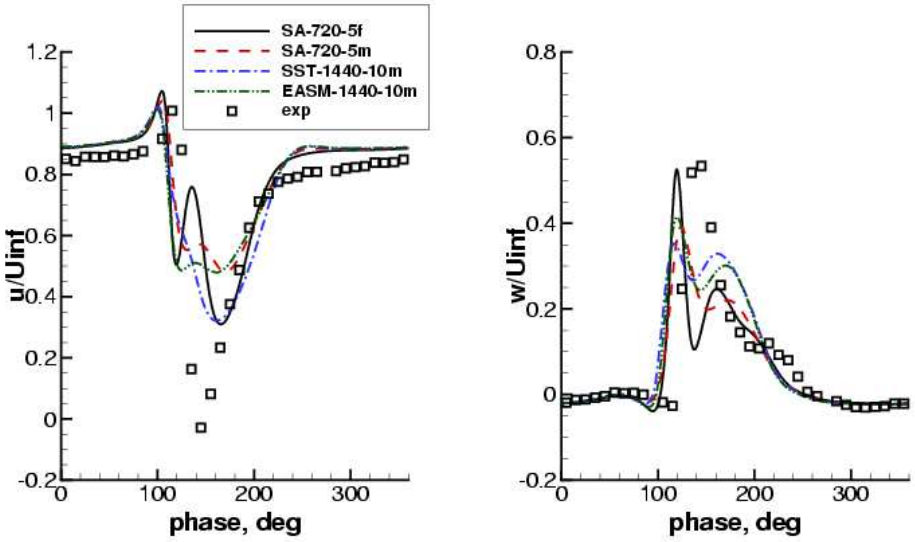

Figure 22: Time history at $x = 63.5$ mm, $y = 0$, $z = 10$ mm (2D downstream).

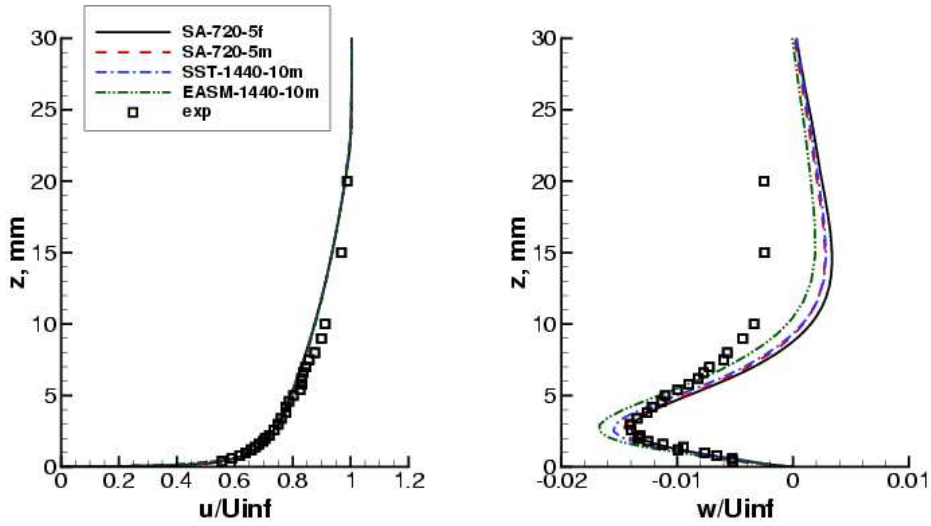

Figure 23: Average velocity at $x = 44.45$ mm, $y = 0$ (1D upstream).

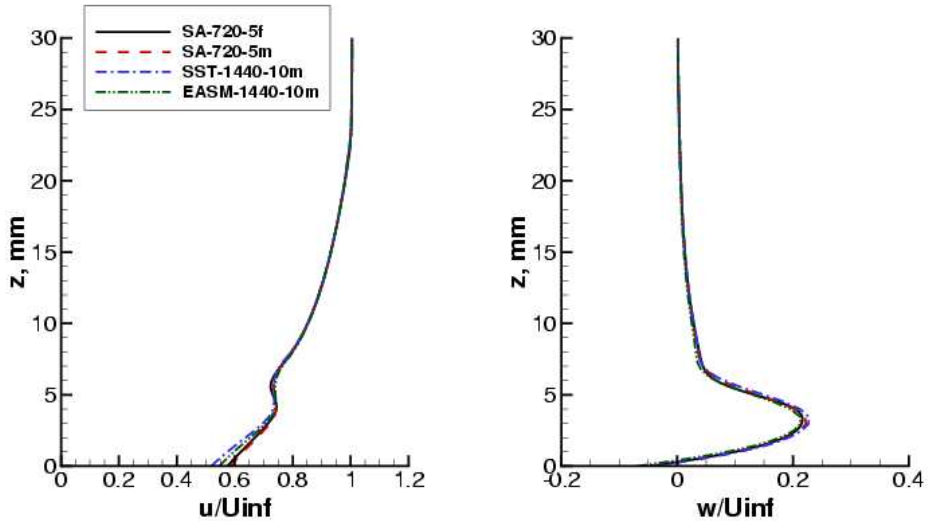

Figure 24: Average velocity at $x = 50.8$ mm, $y = 0$ (over center of orifice).

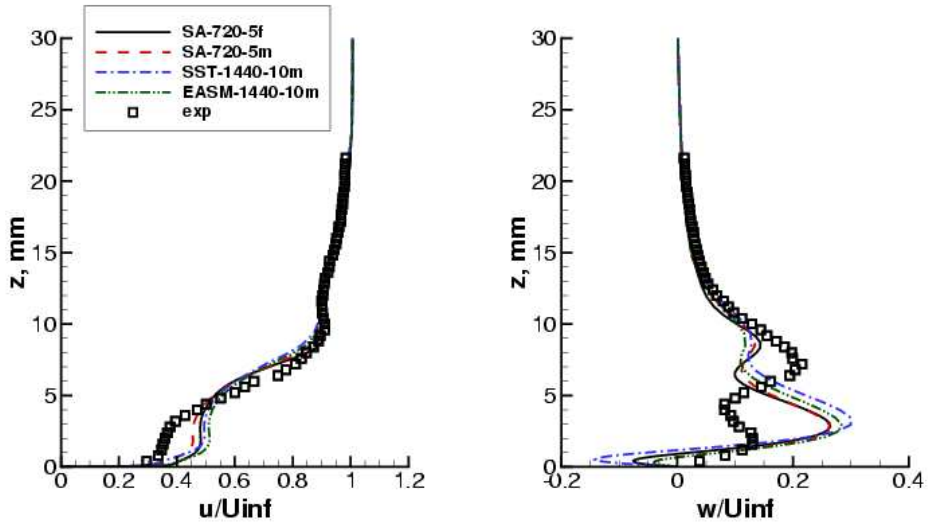

Figure 25: Average velocity at $x = 57.15$ mm, $y = 0$ (1D downstream).

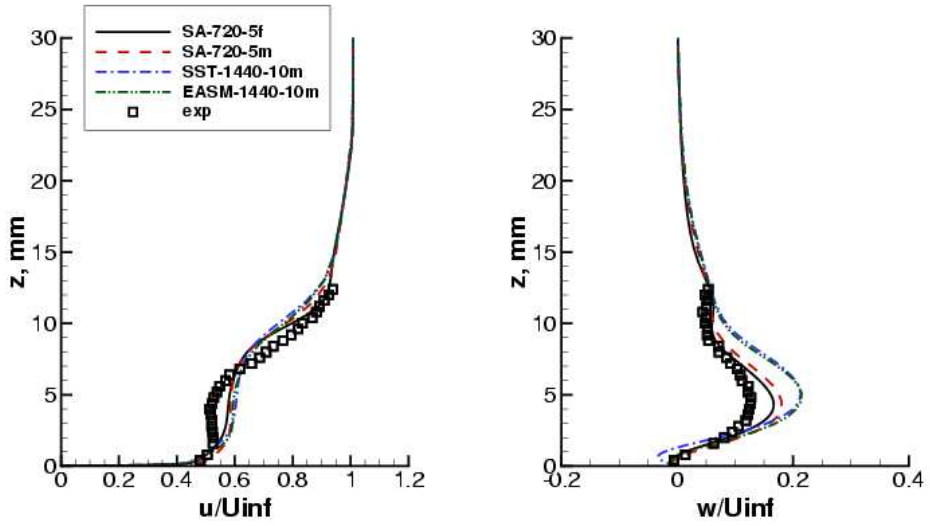

Figure 26: Average velocity at $x = 63.5$ mm, $y = 0$ (2D downstream).

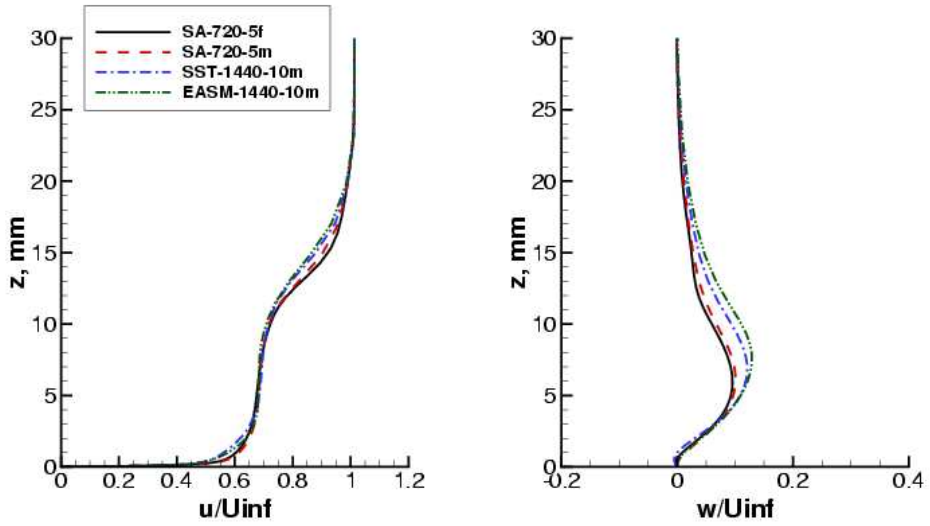

Figure 27: Average velocity at $x = 76.2$ mm, $y = 0$ (4D downstream).

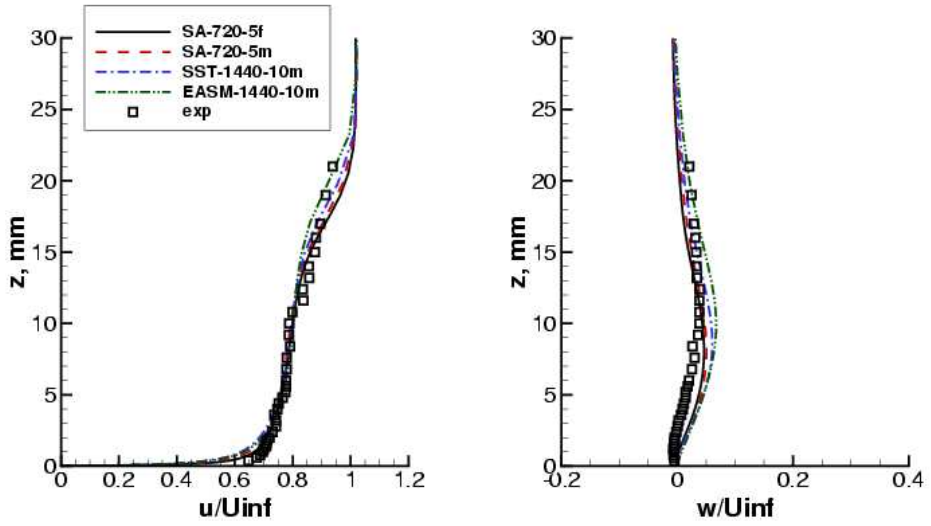

Figure 28: Average velocity at $x = 101.6$ mm, $y = 0$ (8D downstream).

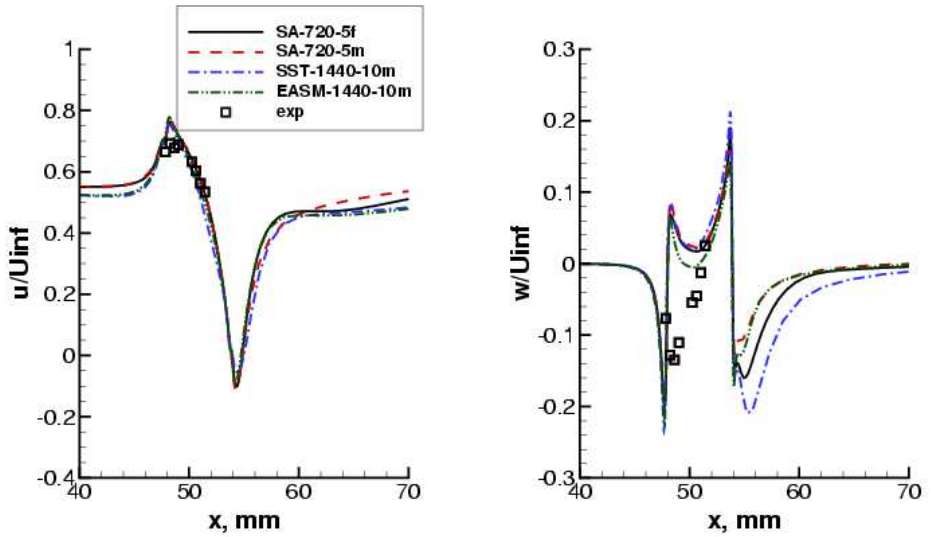

Figure 29: Average velocity at $z = 0.4$ mm, $y = 0$ (along centerplane).

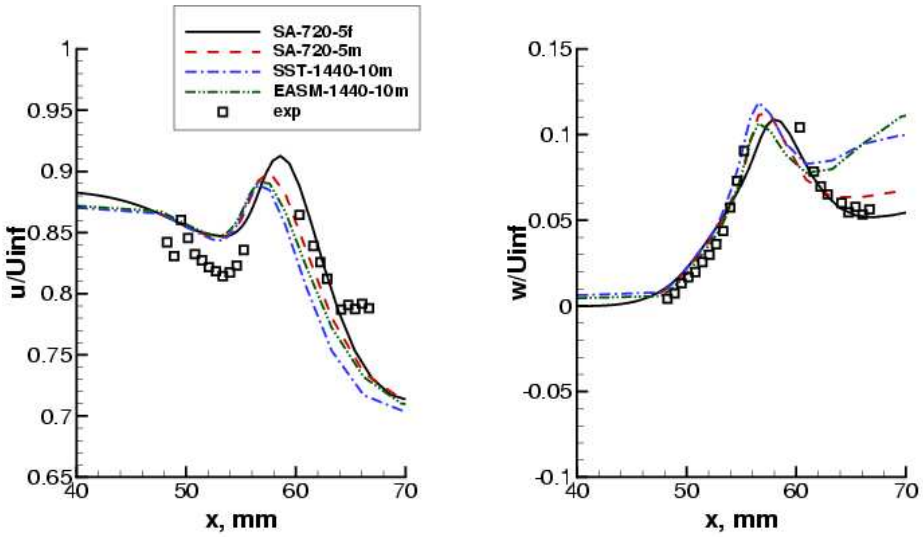

Figure 30: Average velocity at $z = 10$ mm, $y = 0$ (along centerplane).

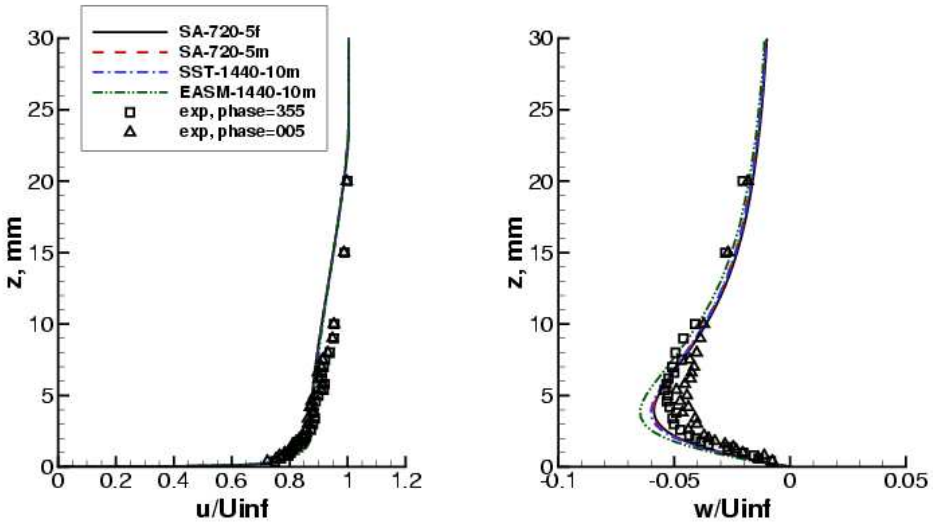

Figure 31: Phase-averaged velocity at $x = 44.45$ mm, $y = 0$ (1D upstream), phase = 0°.

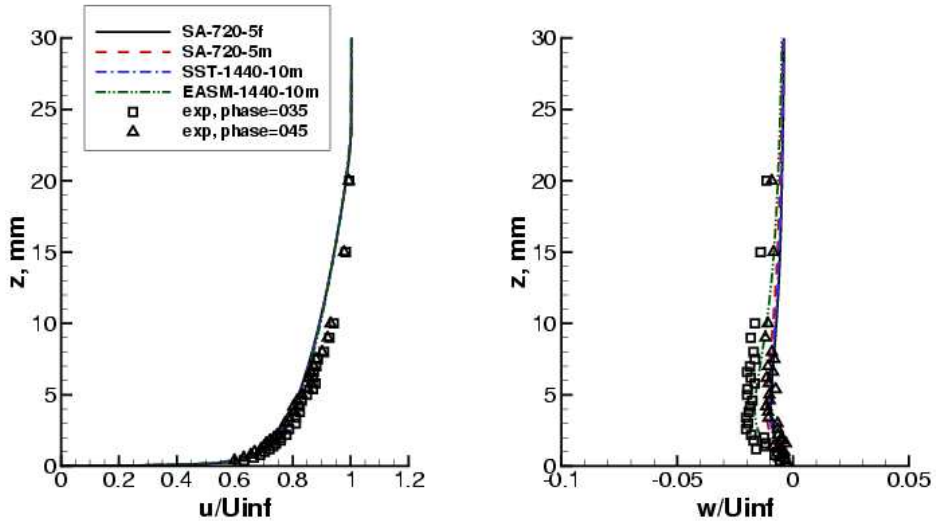

Figure 32: Phase-averaged velocity at $x = 44.45$ mm, $y = 0$ (1D upstream), phase = 40°.

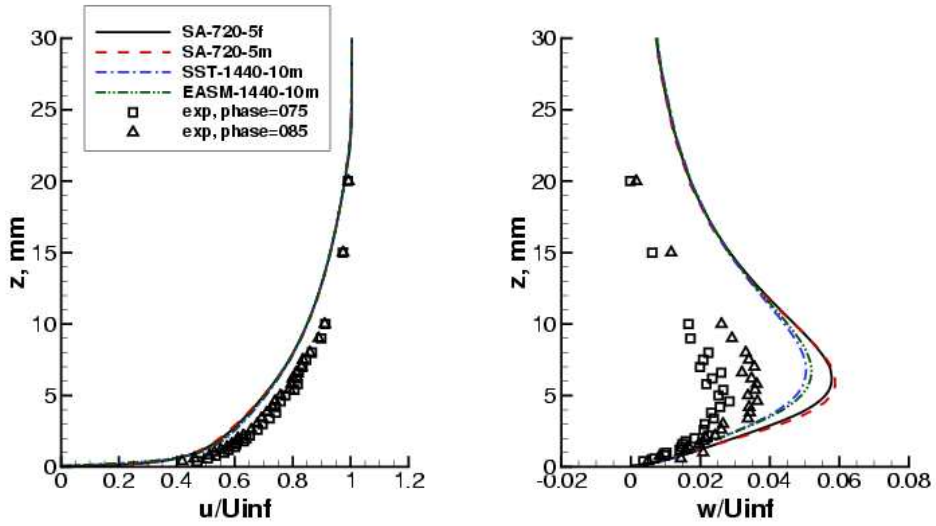

Figure 33: Phase-averaged velocity at $x = 44.45$ mm, $y = 0$ (1D upstream), phase = 80°.

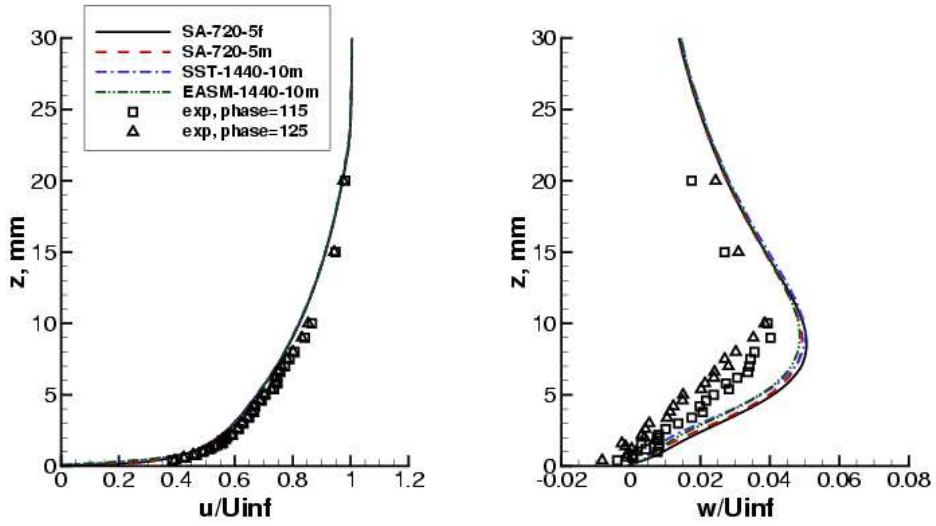

Figure 34: Phase-averaged velocity at $x = 44.45$ mm, $y = 0$ (1D upstream), phase = 120°.

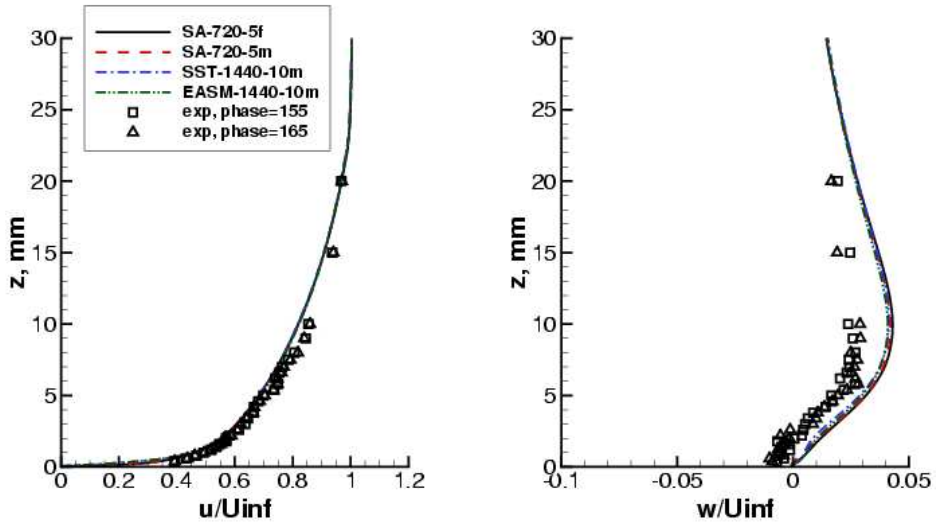

Figure 35: Phase-averaged velocity at $x = 44.45$ mm, $y = 0$ (1D upstream), phase = 160°.

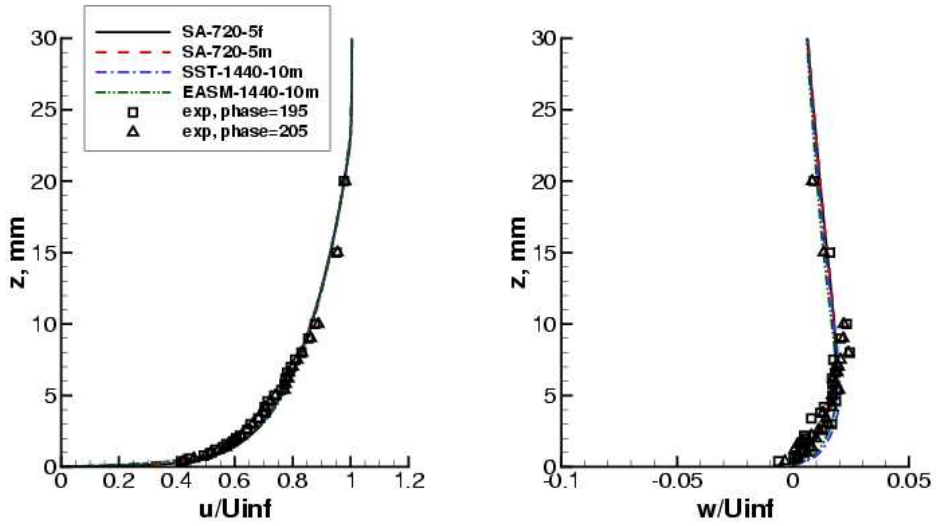

Figure 36: Phase-averaged velocity at $x = 44.45$ mm, $y = 0$ (1D upstream), phase = 200°.

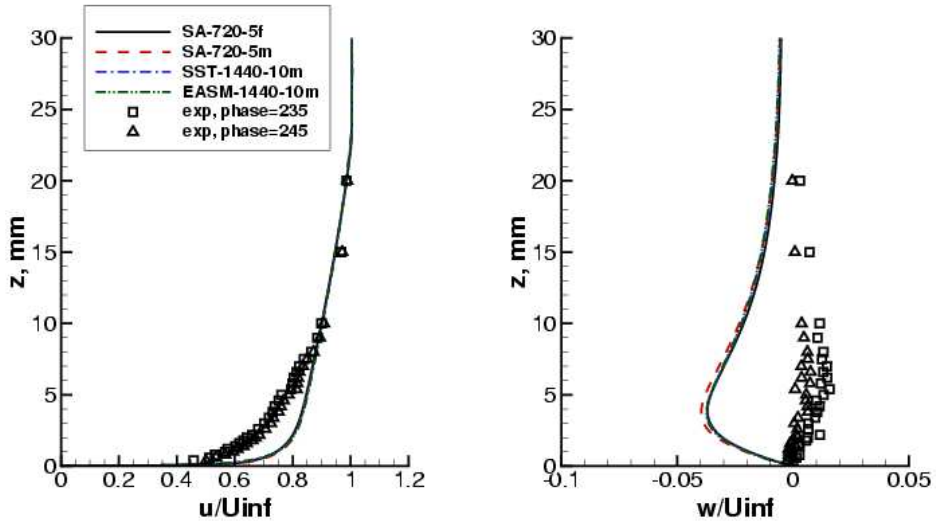

Figure 37: Phase-averaged velocity at $x = 44.45$ mm, $y = 0$ (1D upstream), phase = 240°.

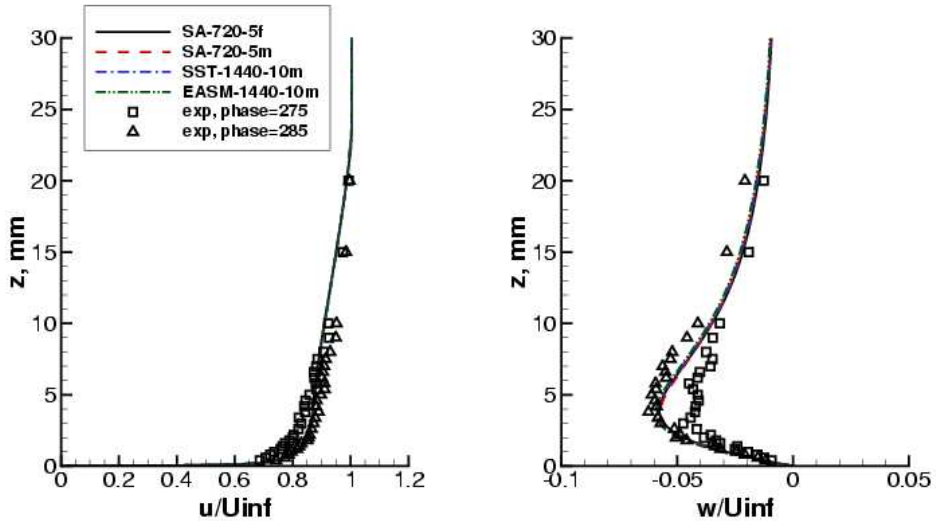

Figure 38: Phase-averaged velocity at $x = 44.45$ mm, $y = 0$ (1D upstream), phase = 280°.

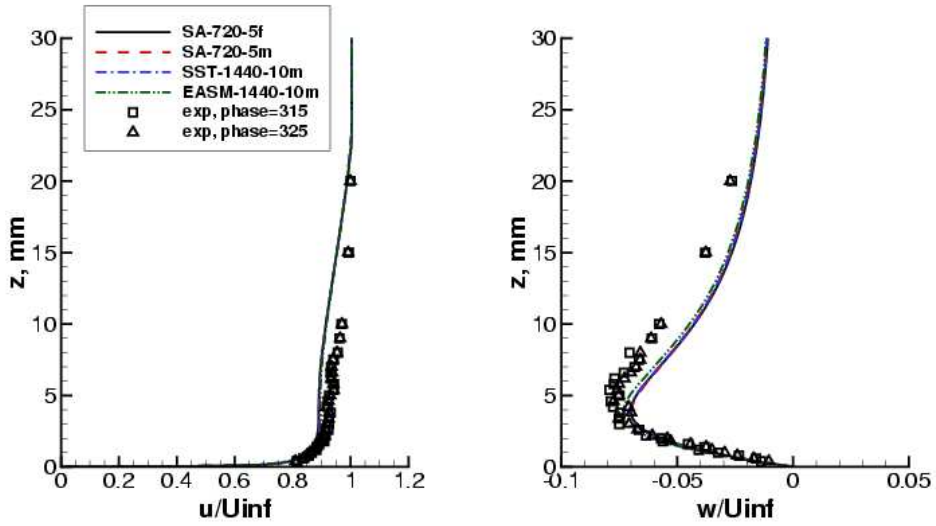

Figure 39: Phase-averaged velocity at $x = 44.45$ mm, $y = 0$ (1D upstream), phase = 320°.

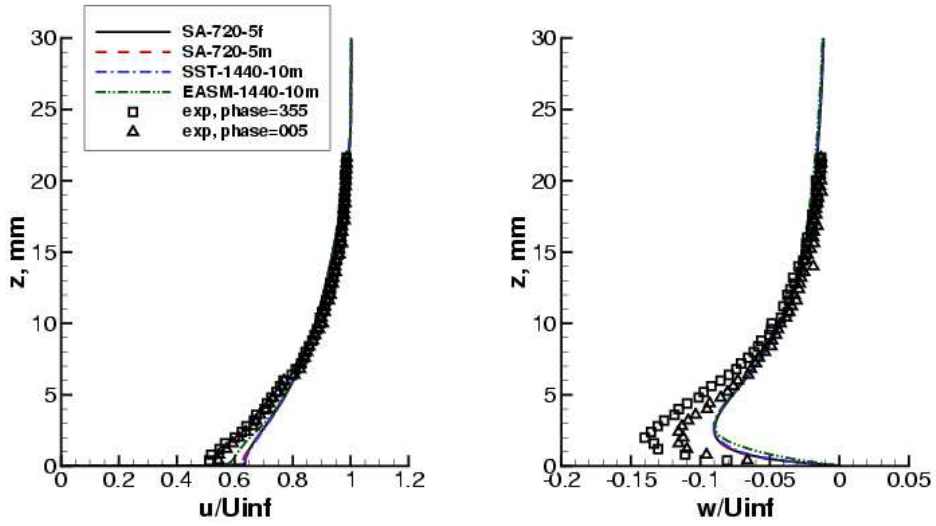

Figure 40: Phase-averaged velocity at $x = 57.15$ mm, $y = 0$ (1D downstream), phase = 0°.

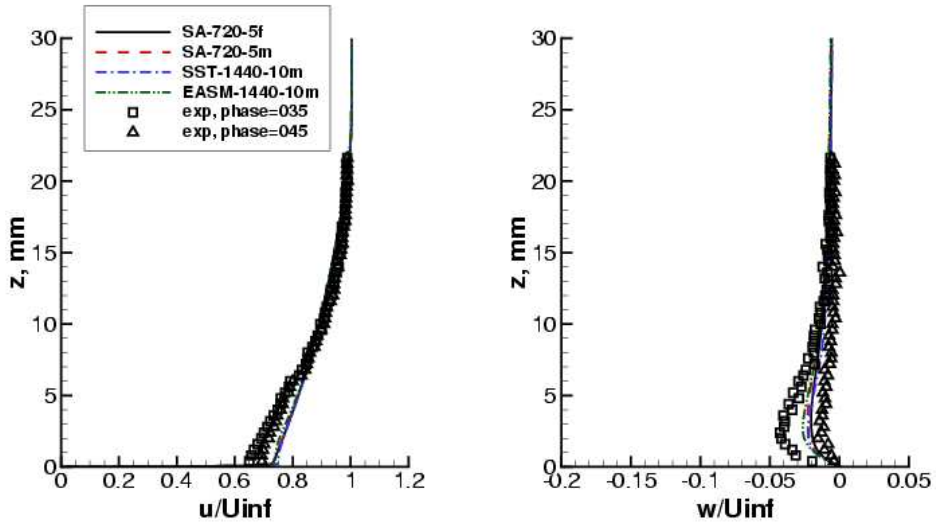

Figure 41: Phase-averaged velocity at $x = 57.15$ mm, $y = 0$ (1D downstream), phase = 40°.

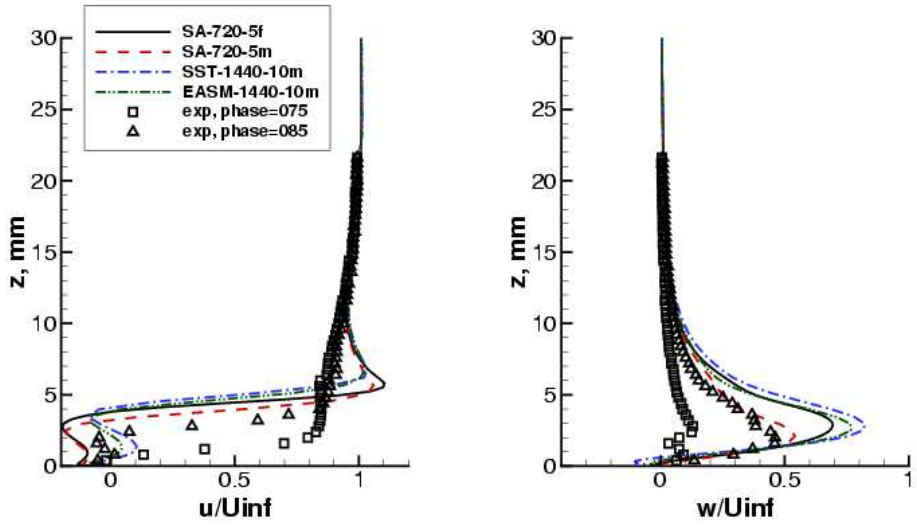

Figure 42: Phase-averaged velocity at $x = 57.15$ mm, $y = 0$ (1D downstream), phase = 80°.

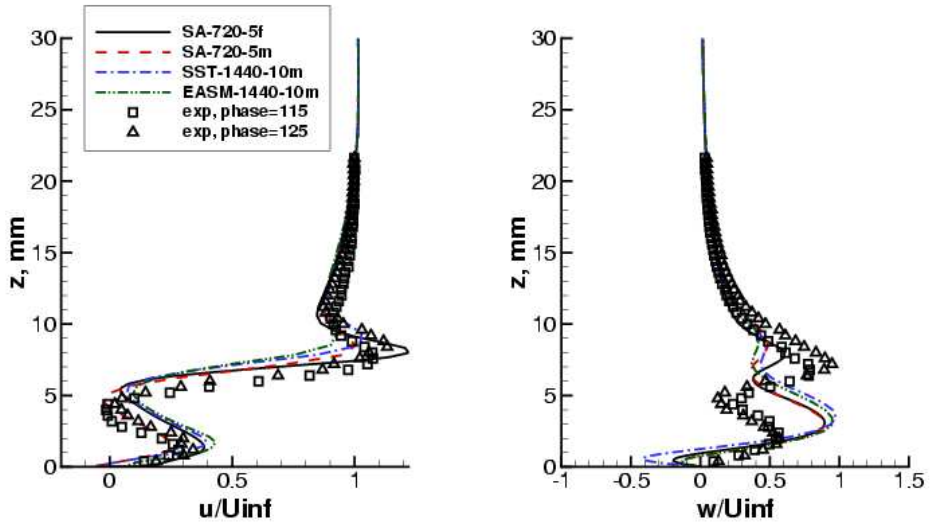

Figure 43: Phase-averaged velocity at $x = 57.15$ mm, $y = 0$ (1D downstream), phase = 120°.

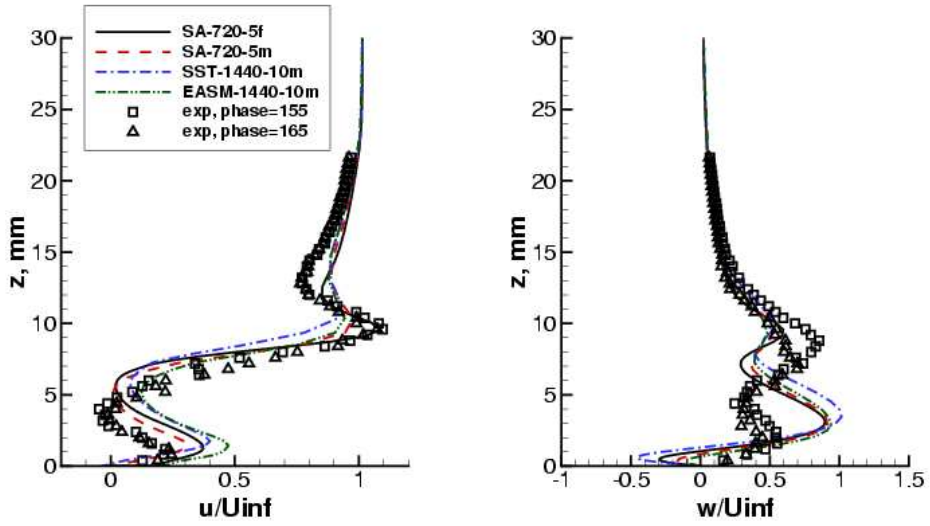

Figure 44: Phase-averaged velocity at $x = 57.15$ mm, $y = 0$ (1D downstream), phase = 160°.

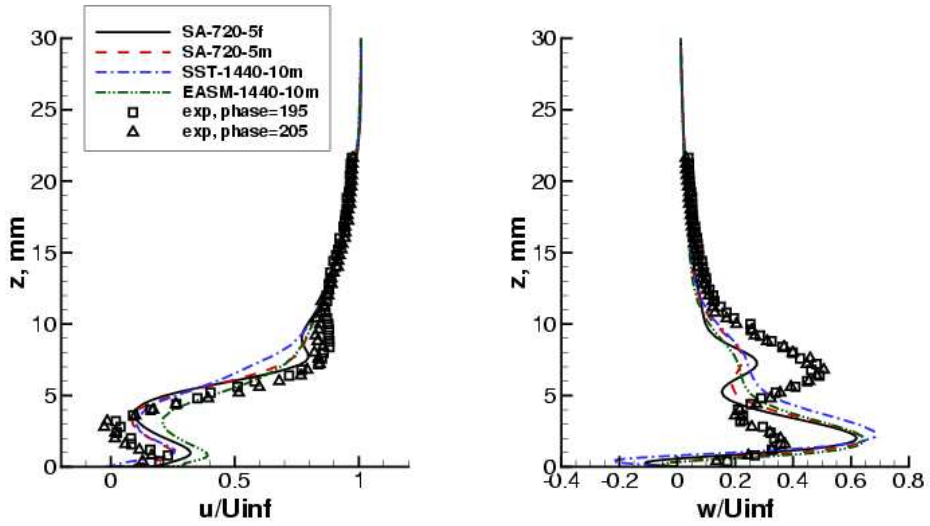

Figure 45: Phase-averaged velocity at $x = 57.15$ mm, $y = 0$ (1D downstream), phase = 200°.

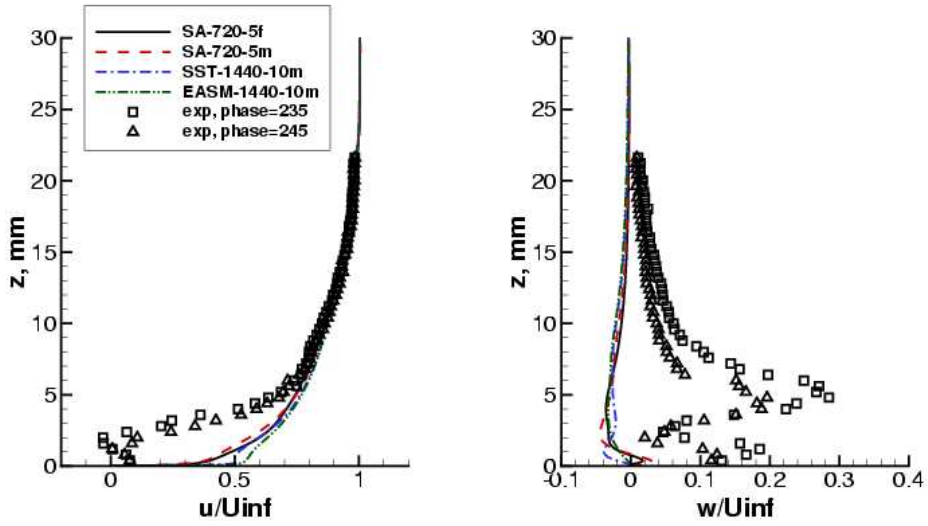

Figure 46: Phase-averaged velocity at $x = 57.15$ mm, $y = 0$ (1D downstream), phase = 240°.

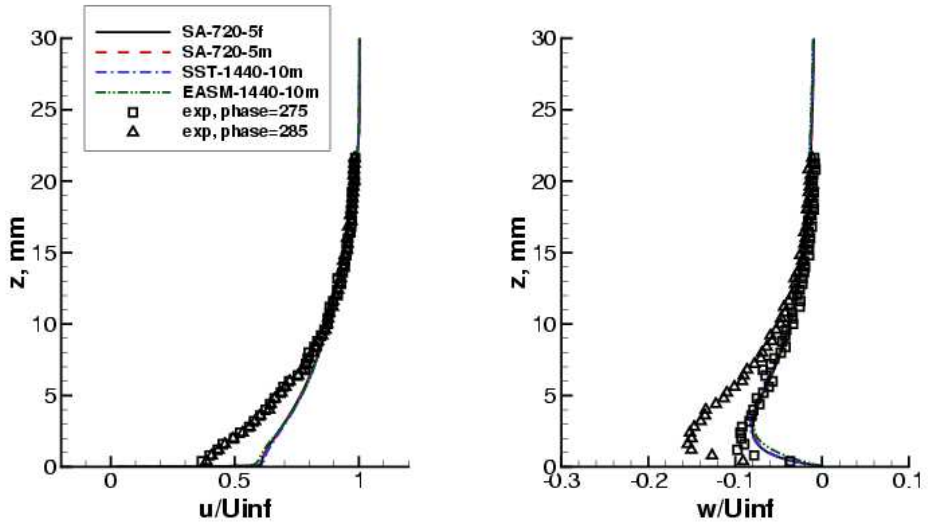

Figure 47: Phase-averaged velocity at $x = 57.15$ mm, $y = 0$ (1D downstream), phase = 280°.

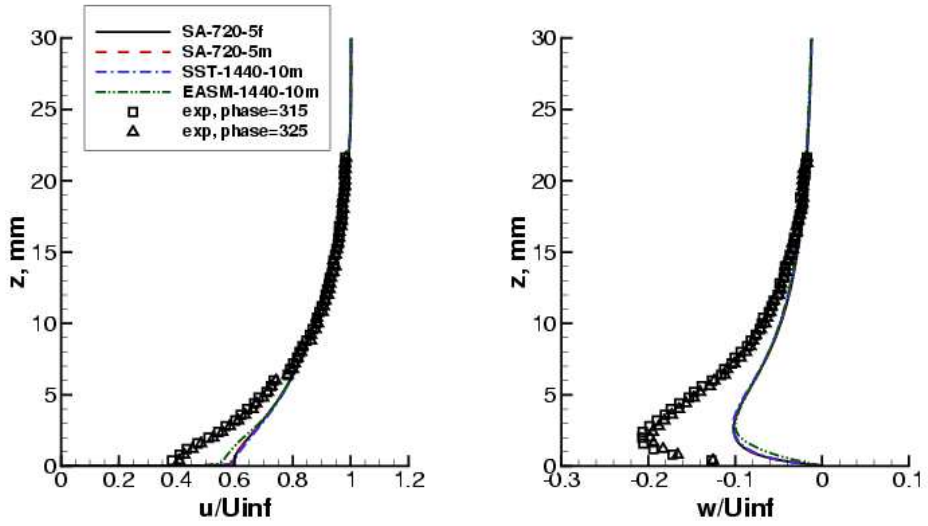

Figure 48: Phase-averaged velocity at $x = 57.15$ mm, $y = 0$ (1D downstream), phase = 320°.

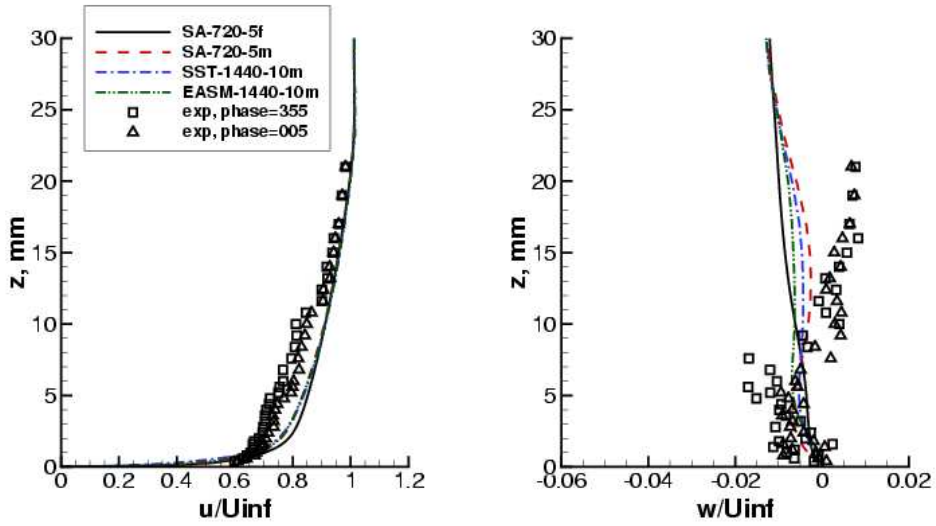

Figure 49: Phase-averaged velocity at $x = 101.6$ mm, $y = 0$ (8D downstream), phase = 0°.

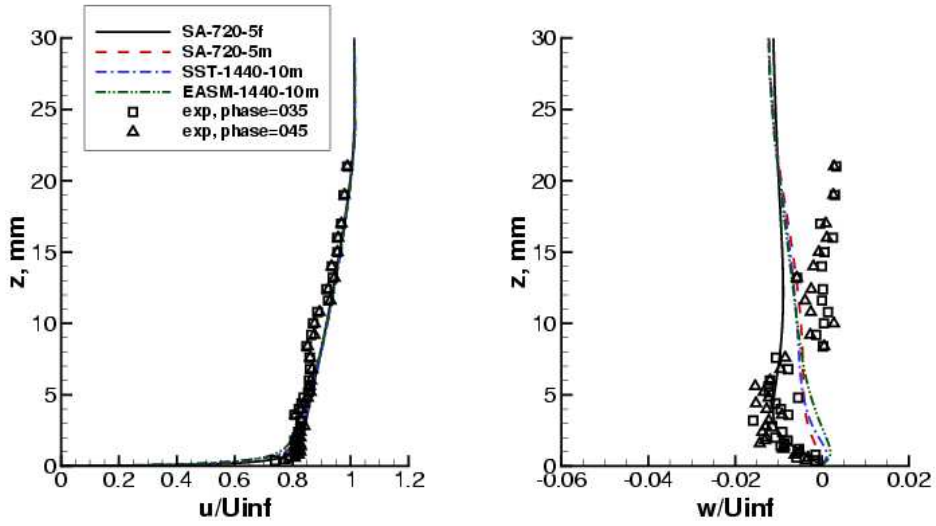

Figure 50: Phase-averaged velocity at $x = 101.6$ mm, $y = 0$ (8D downstream), phase = 40°.

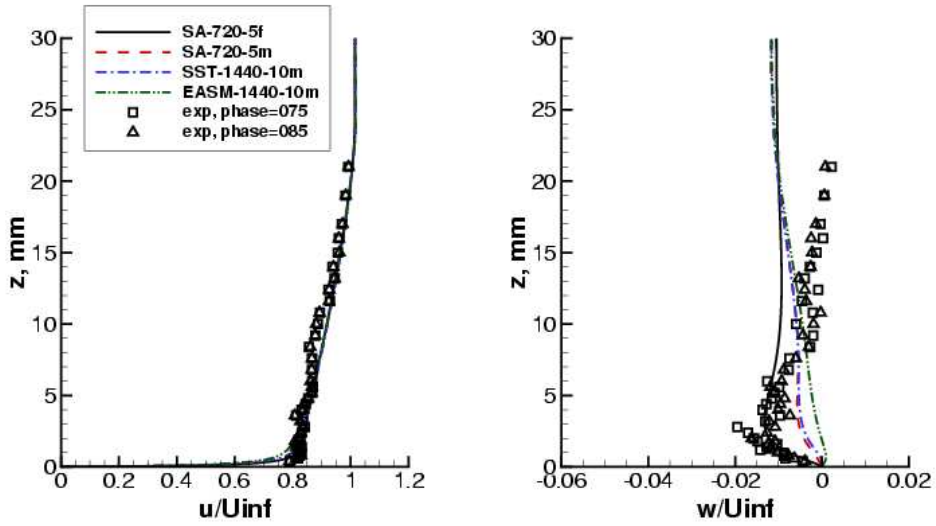

Figure 51: Phase-averaged velocity at $x = 101.6$ mm, $y = 0$ (8D downstream), phase = 80°.

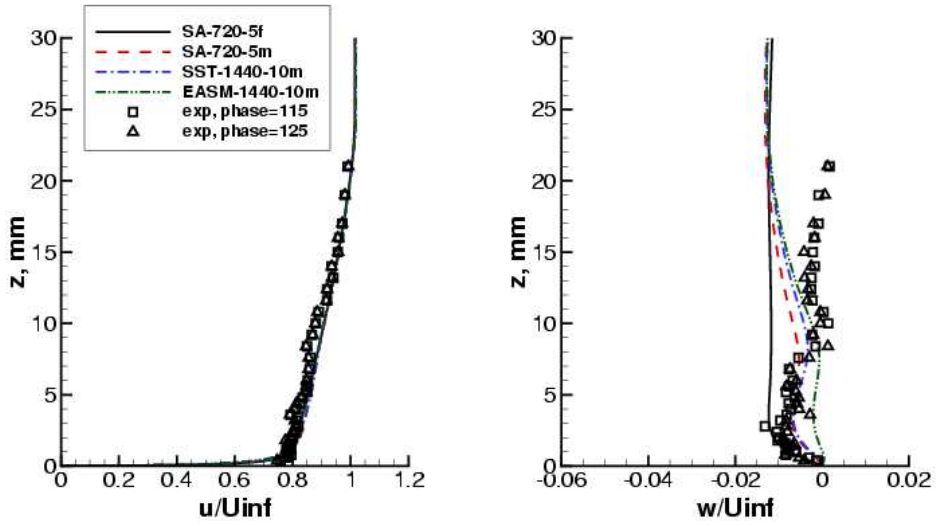

Figure 52: Phase-averaged velocity at $x = 101.6$ mm, $y = 0$ (8D downstream), phase = 120°.

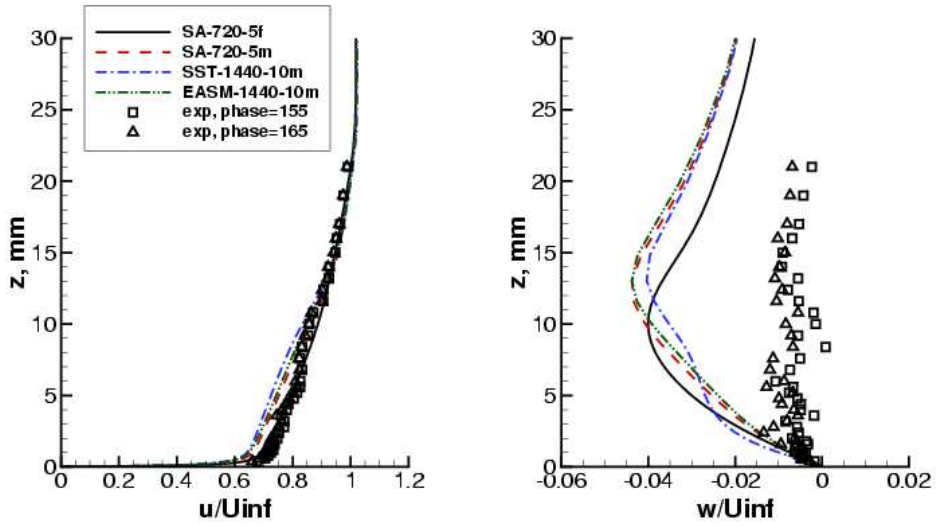

Figure 53: Phase-averaged velocity at $x = 101.6$ mm, $y = 0$ (8D downstream), phase = 160°.

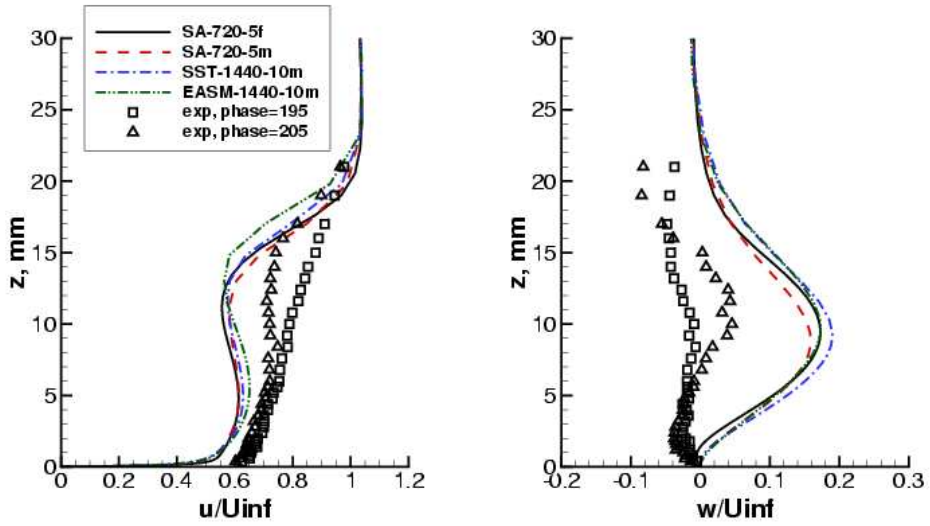

Figure 54: Phase-averaged velocity at $x = 101.6$ mm, $y = 0$ (8D downstream), phase = 200°.

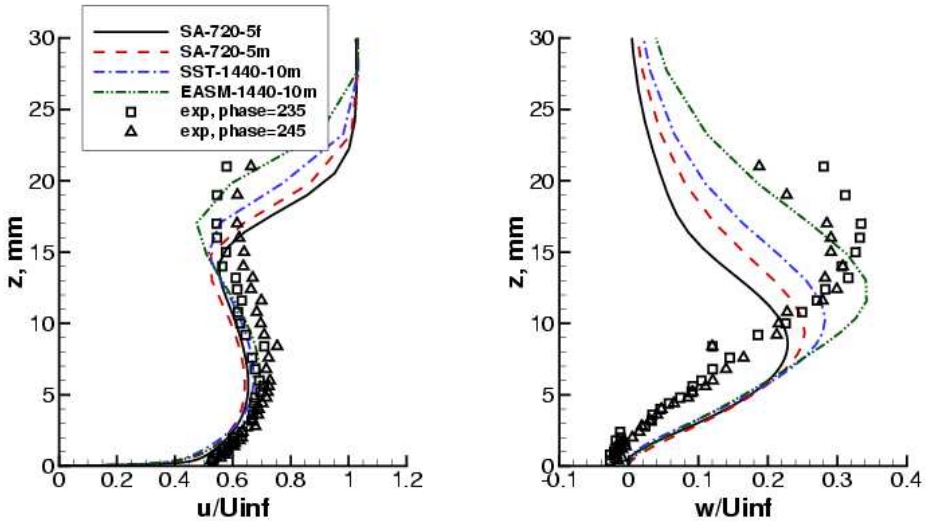

Figure 55: Phase-averaged velocity at $x = 101.6$ mm, $y = 0$ (8D downstream), phase = 240°.

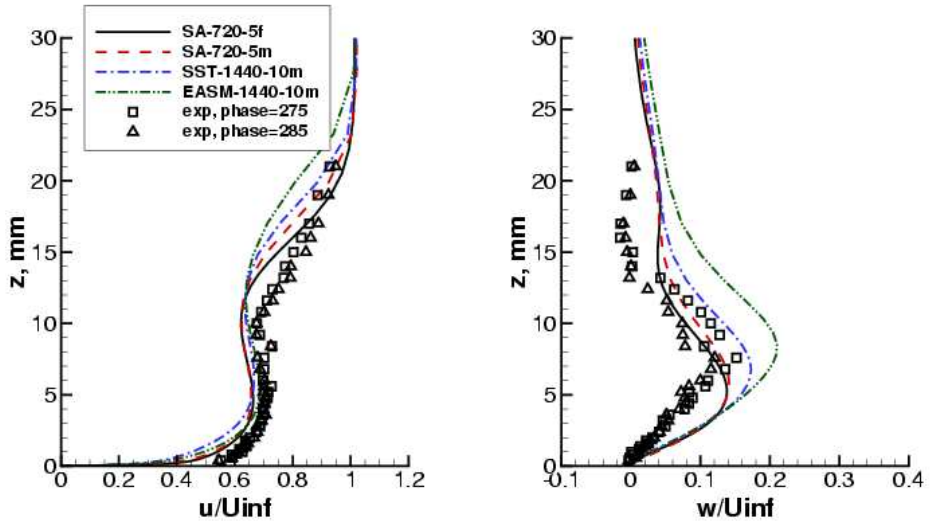

Figure 56: Phase-averaged velocity at $x = 101.6$ mm, $y = 0$ (8D downstream), phase = 280°.

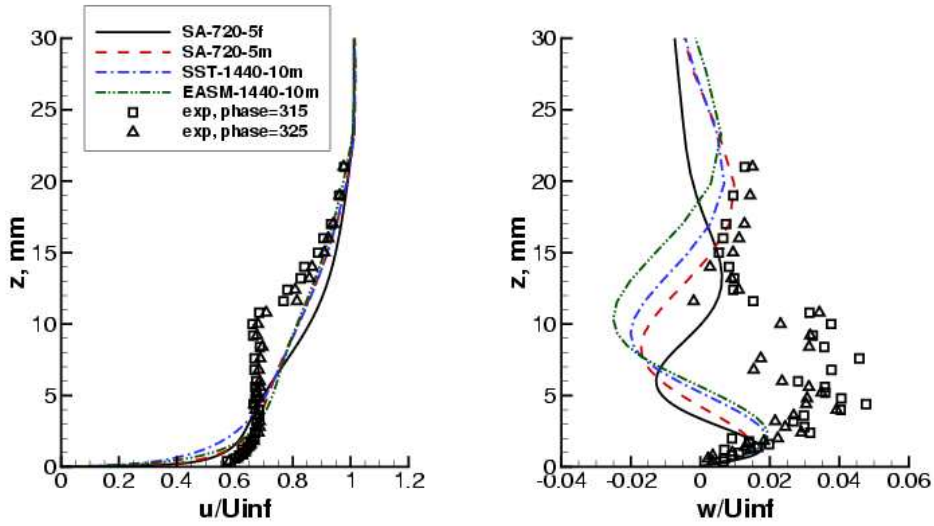

Figure 57: Phase-averaged velocity at $x = 101.6$ mm, $y = 0$ (8D downstream), phase = 320°.

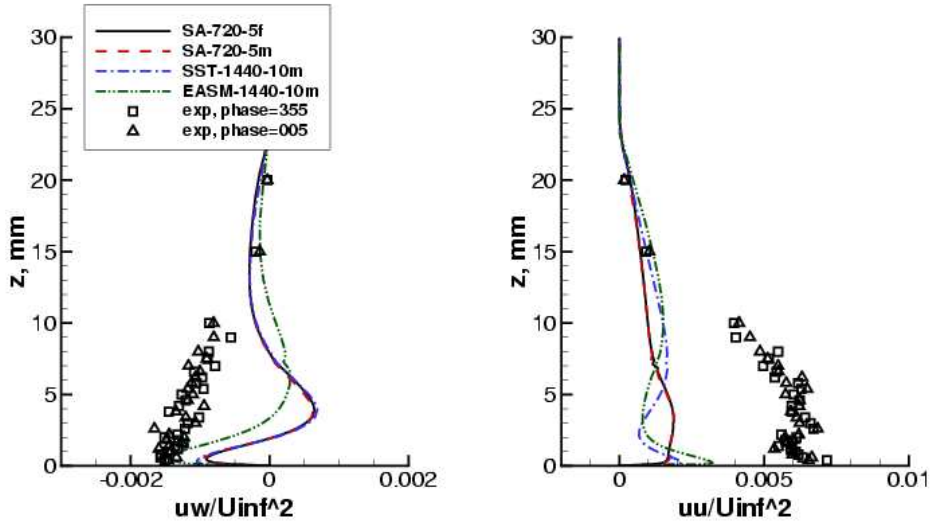

Figure 58: Phase-averaged turbulence quantities at $x = 44.45$ mm, $y = 0$ (1D upstream), phase $= 0°$.

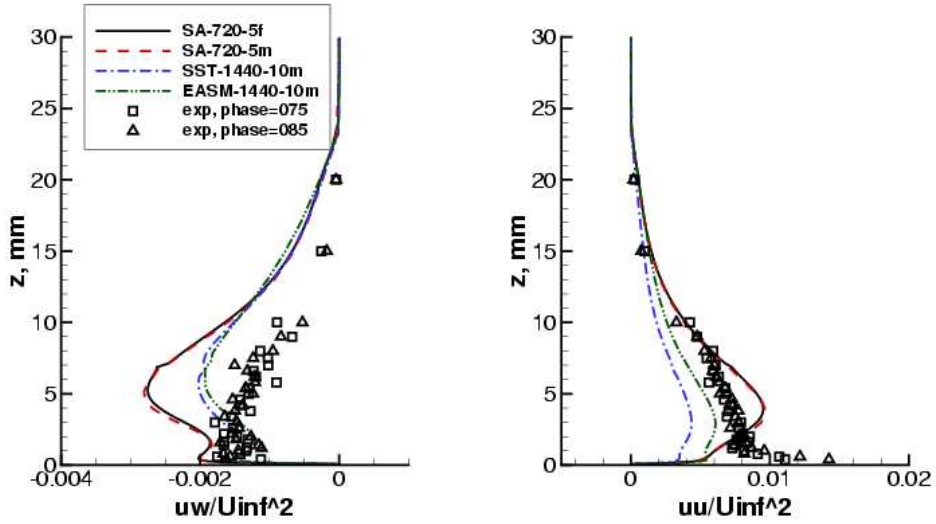

Figure 59: Phase-averaged turbulence quantities at $x = 44.45$ mm, $y = 0$ (1D upstream), phase $= 80°$.

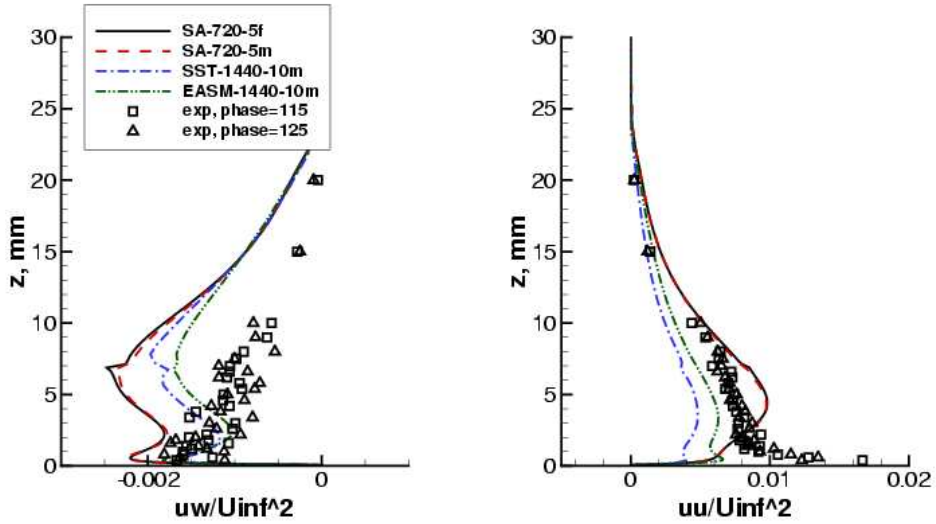

Figure 60: Phase-averaged turbulence quantities at $x = 44.45$ mm, $y = 0$ (1D upstream), phase = 120°.

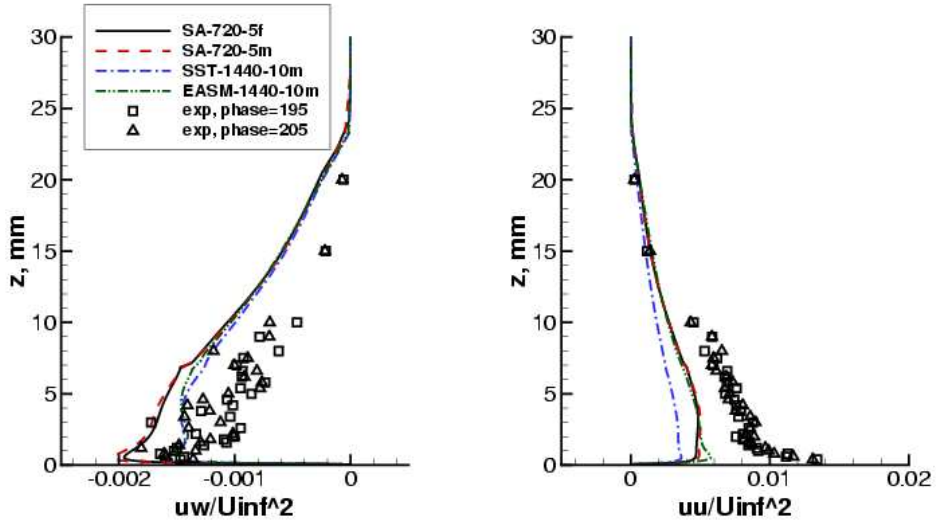

Figure 61: Phase-averaged turbulence quantities at $x = 44.45$ mm, $y = 0$ (1D upstream), phase = 200°.

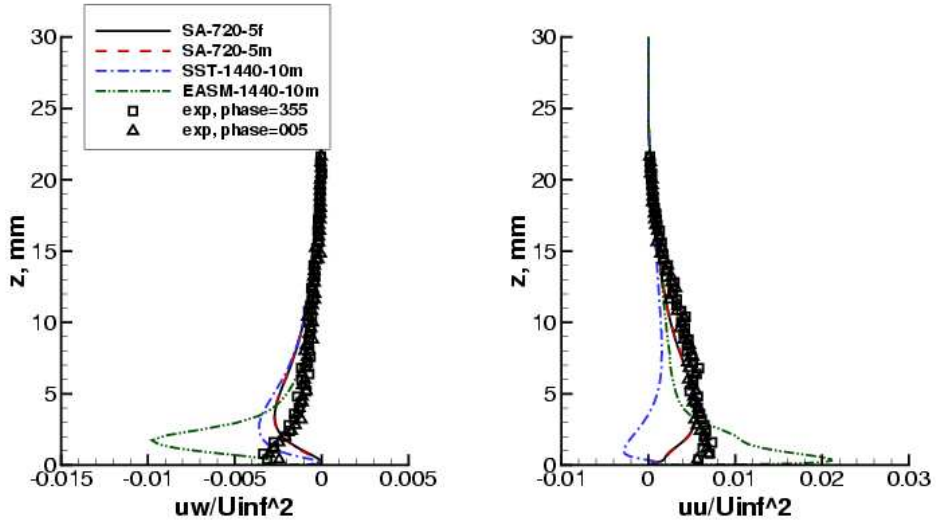

Figure 62: Phase-averaged turbulence quantities at $x = 57.15$ mm, $y = 0$ (1D downstream), phase = 0°.

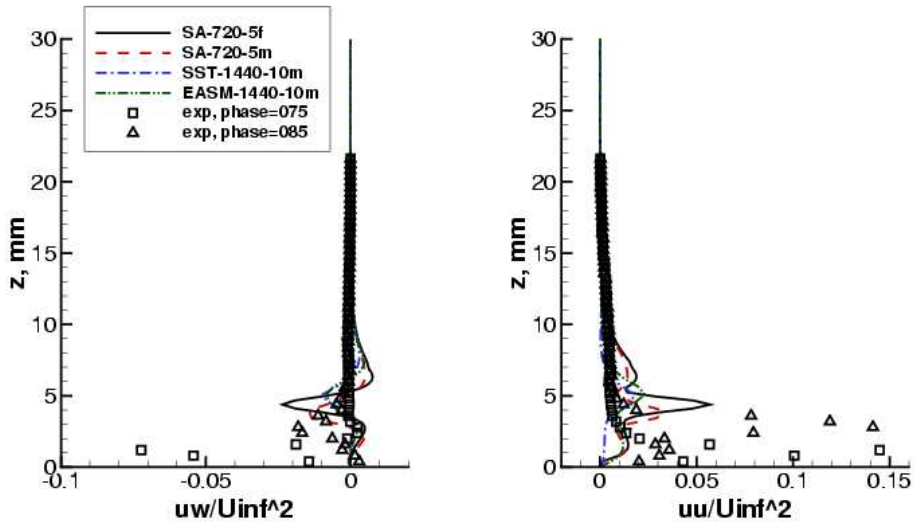

Figure 63: Phase-averaged turbulence quantities at $x = 57.15$ mm, $y = 0$ (1D downstream), phase = 80°.

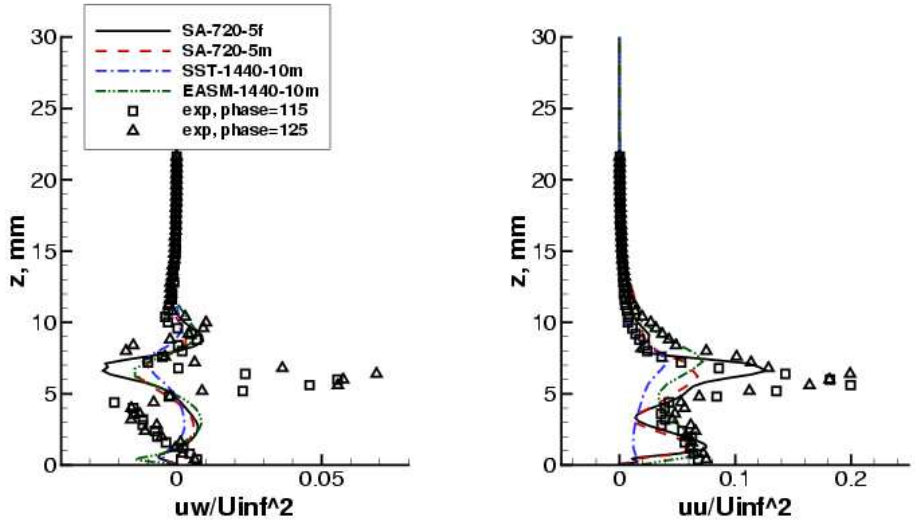

Figure 64: Phase-averaged turbulence quantities at $x = 57.15$ mm, $y = 0$ (1D downstream), phase = 120°.

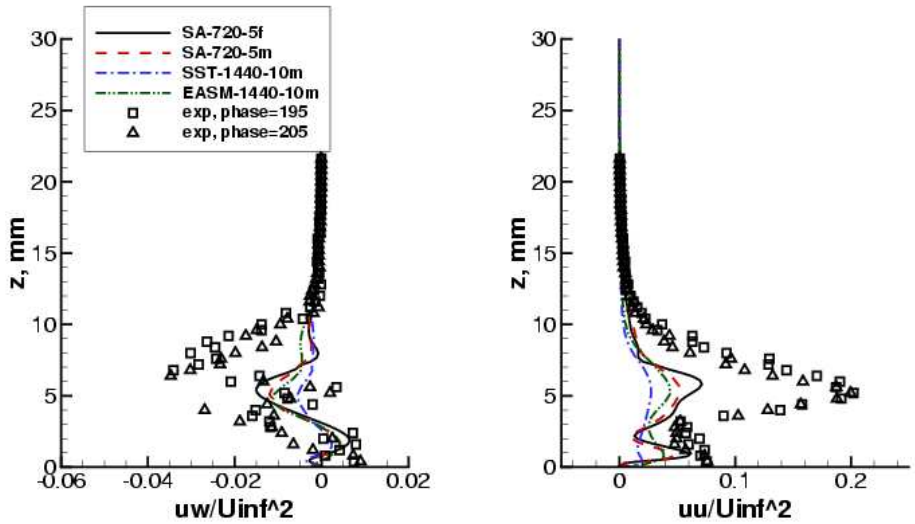

Figure 65: Phase-averaged turbulence quantities at $x = 57.15$ mm, $y = 0$ (1D downstream), phase = 200°.

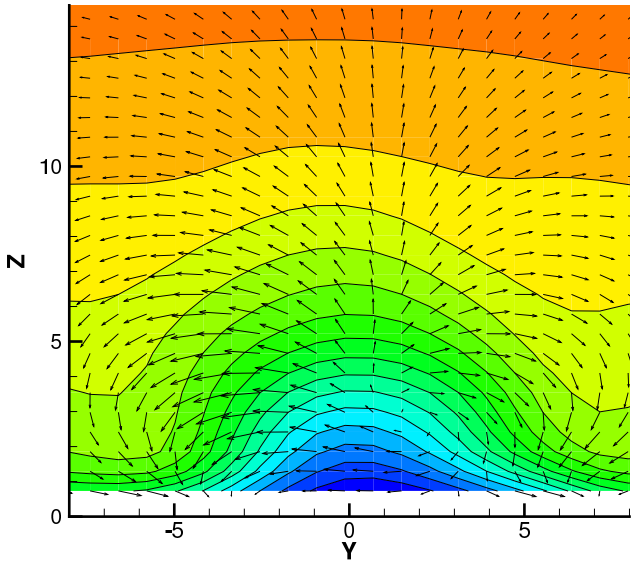

Figure 66: Experimental contours of long-time-average u-velocity along with in-plane velocity vectors 1D downstream.

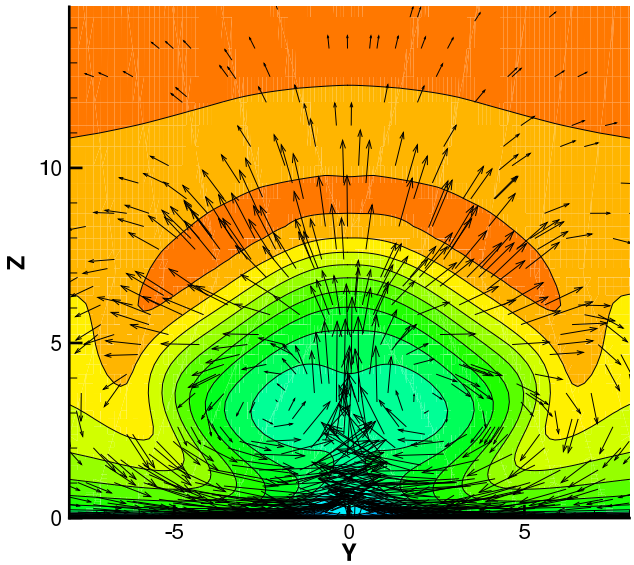

Figure 67: Contours of long-time-average u-velocity along with in-plane velocity vectors 1D downstream, using SA model on fine grid.

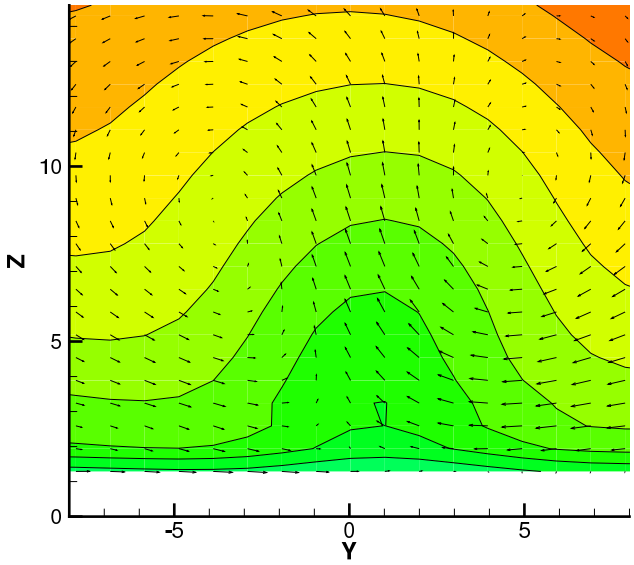

Figure 68: Experimental contours of long-time-average u-velocity along with in-plane velocity vectors 4D downstream.

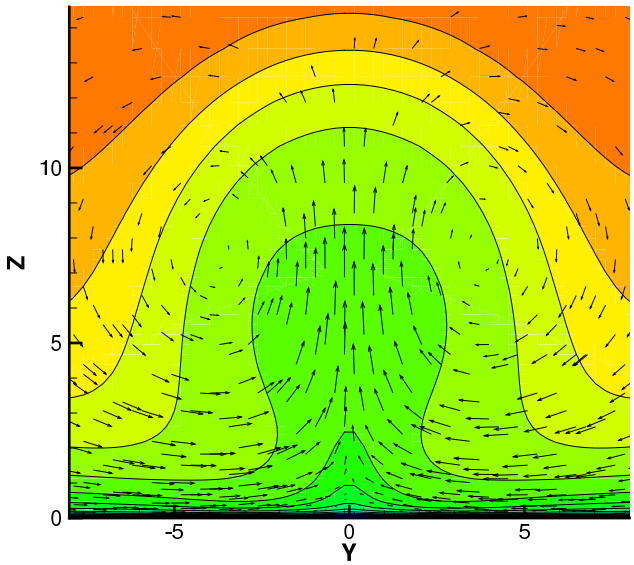

Figure 69: Contours of long-time-average u-velocity along with in-plane velocity vectors 4D downstream, using SA model on fine grid.

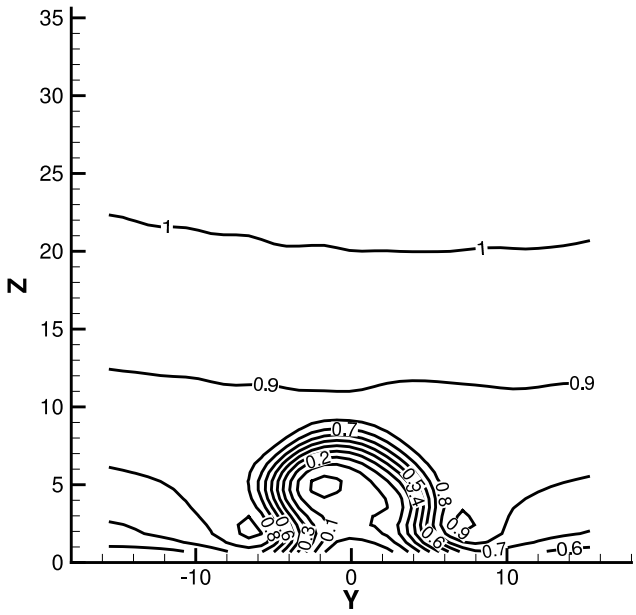

Figure 70: Experimental contours of u-velocity in the plane 1D downstream at phase = 120°.

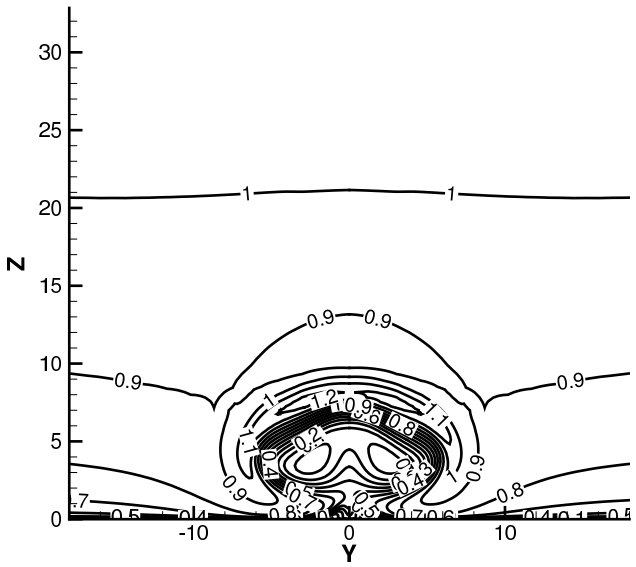

Figure 71: Contours of u-velocity in the plane 1D downstream at phase = 120°, using SA model on fine grid.

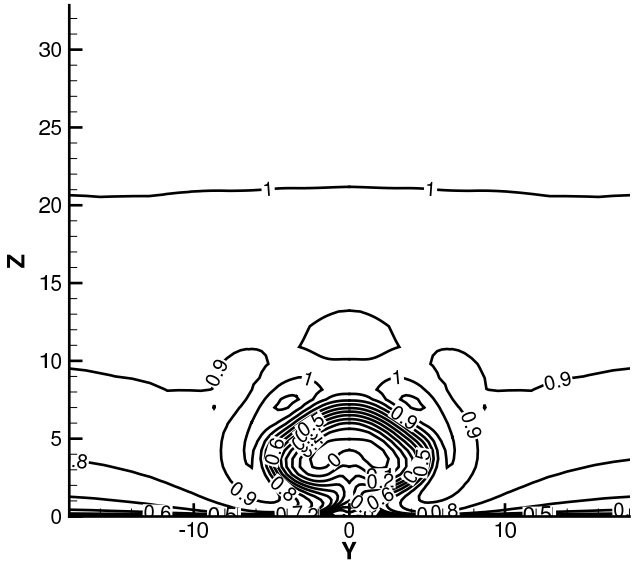

Figure 72: Contours of u-velocity in the plane 1D downstream at phase = 120°, using SA model on medium grid.

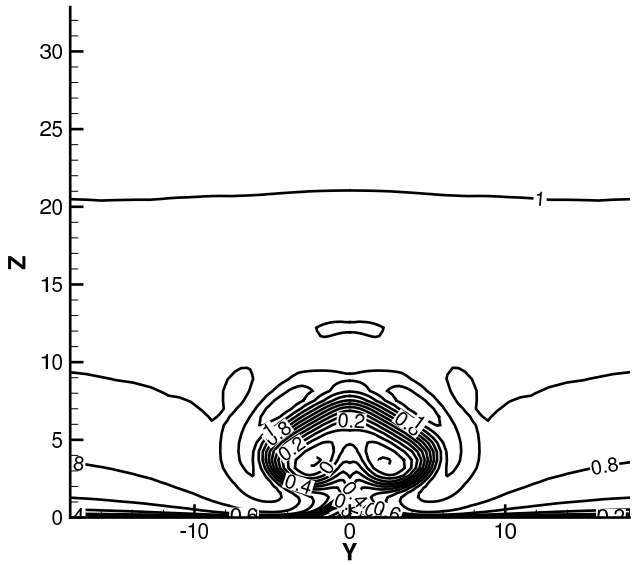

Figure 73: Contours of u-velocity in the plane 1D downstream at phase = 120°, using SST model on medium grid.

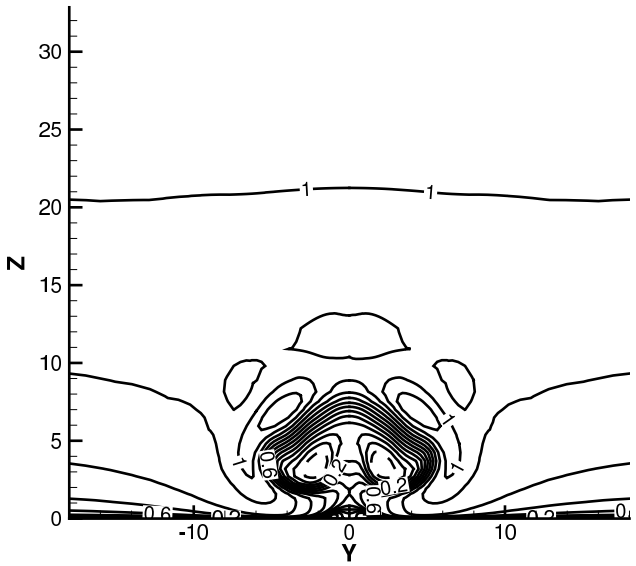

Figure 74: Contours of u-velocity in the plane 1D downstream at phase = 120°, using EASM-ko model on medium grid.

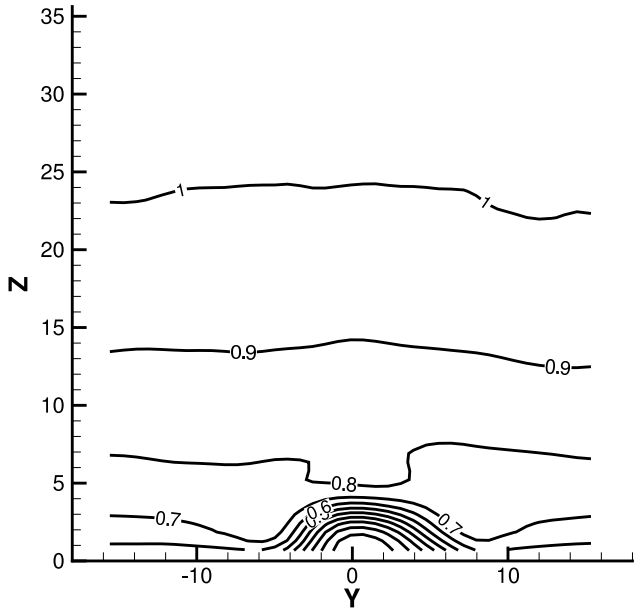

Figure 75: Experimental contours of u-velocity in the plane 1D downstream at phase = 200°.

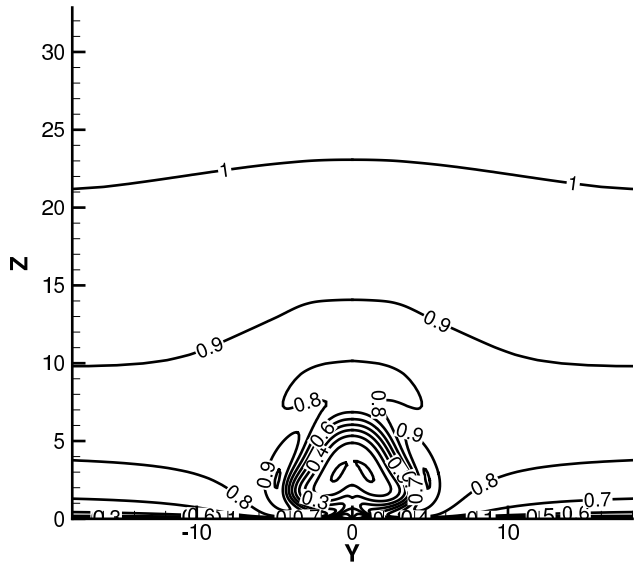

Figure 76: Contours of u-velocity in the plane 1D downstream at phase = 200°, using SA model on fine grid.

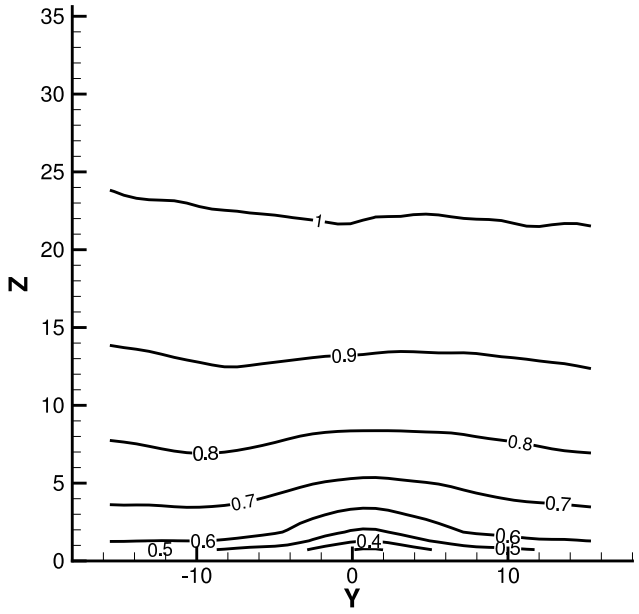

Figure 77: Experimental contours of u-velocity in the plane 1D downstream at phase = 280°.

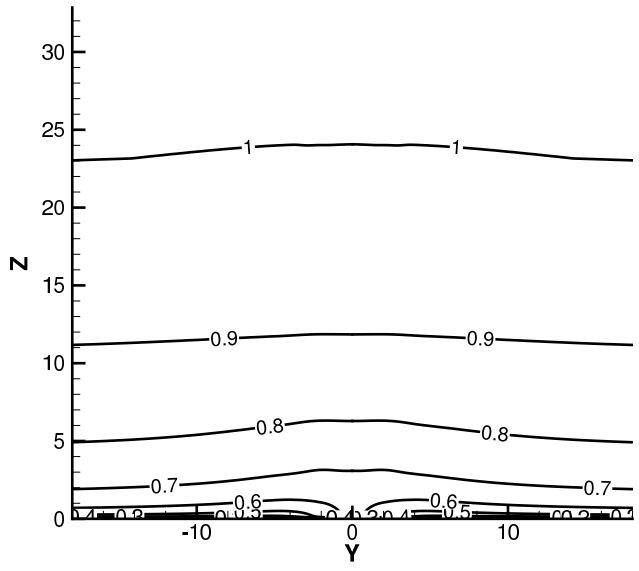

Figure 78: Contours of u-velocity in the plane 1D downstream at phase = 280°, using SA model on fine grid.

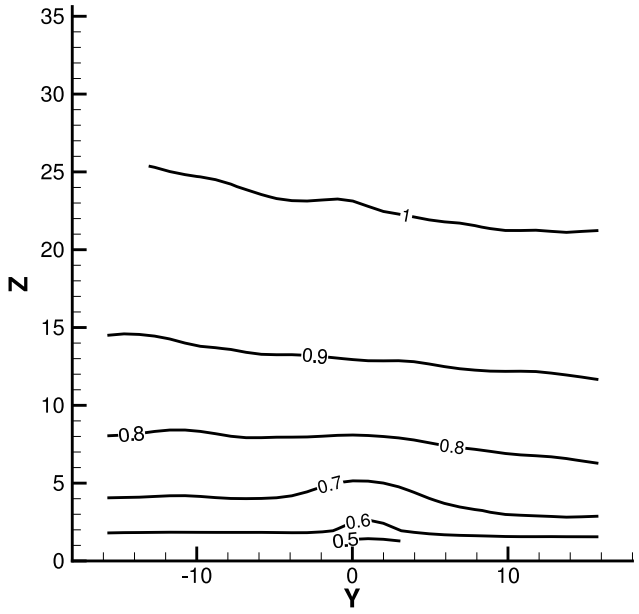

Figure 79: Experimental contours of u-velocity in the plane 4D downstream at phase = 120°.

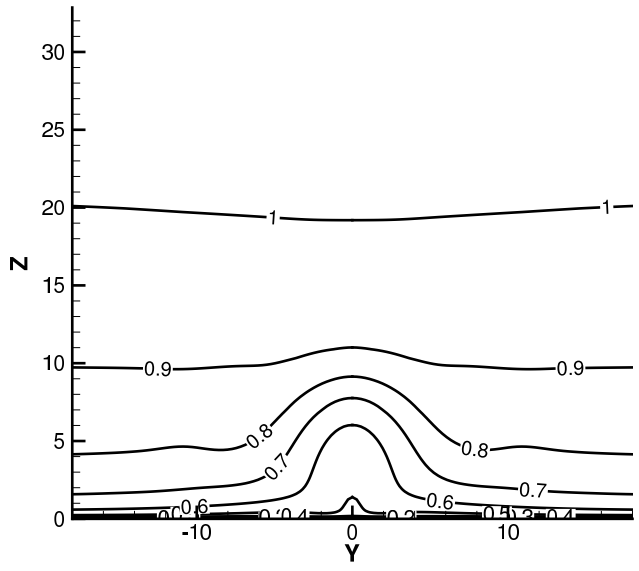

Figure 80: Contours of u-velocity in the plane 4D downstream at phase = 120°, using SA model on fine grid.

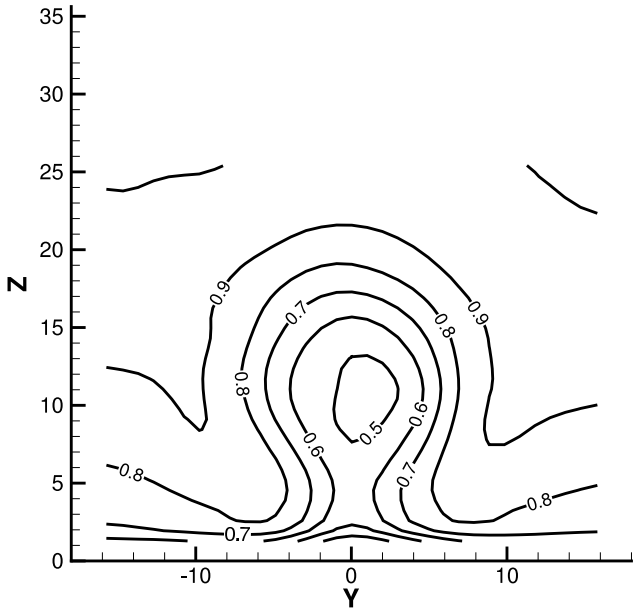

Figure 81: Experimental contours of u-velocity in the plane 4D downstream at phase = 200°.

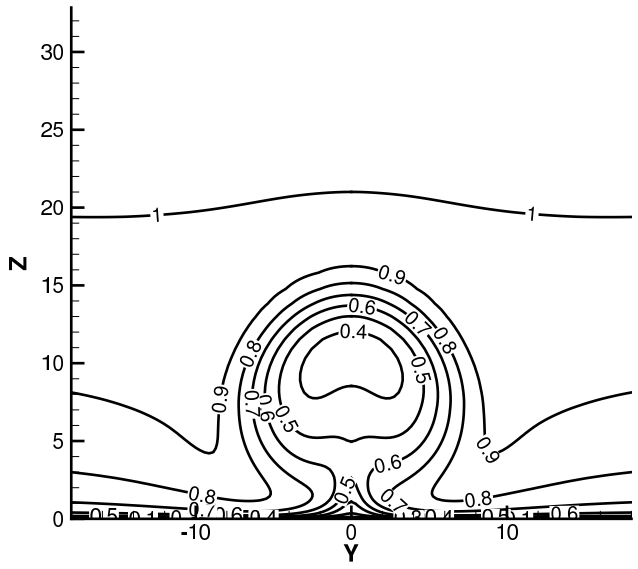

Figure 82: Contours of u-velocity in the plane 4D downstream at phase = 200°, using SA model on fine grid.

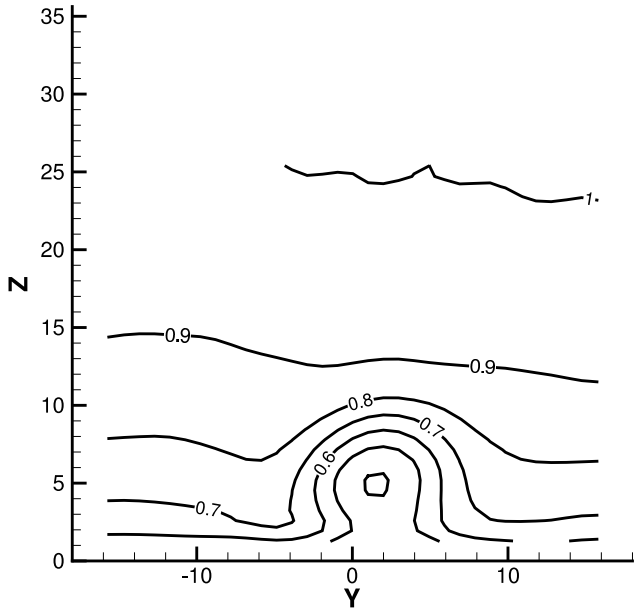

Figure 83: Experimental contours of u-velocity in the plane 4D downstream at phase = 280°.

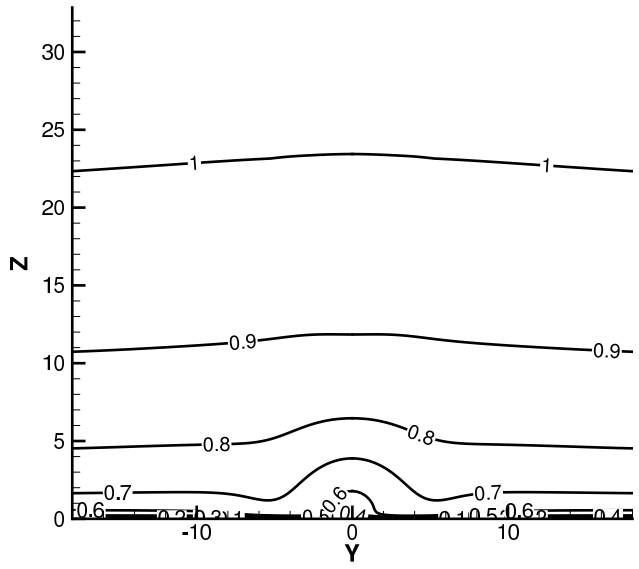

Figure 84: Contours of u-velocity in the plane 4D downstream at phase = 280°, using SA model on fine grid.

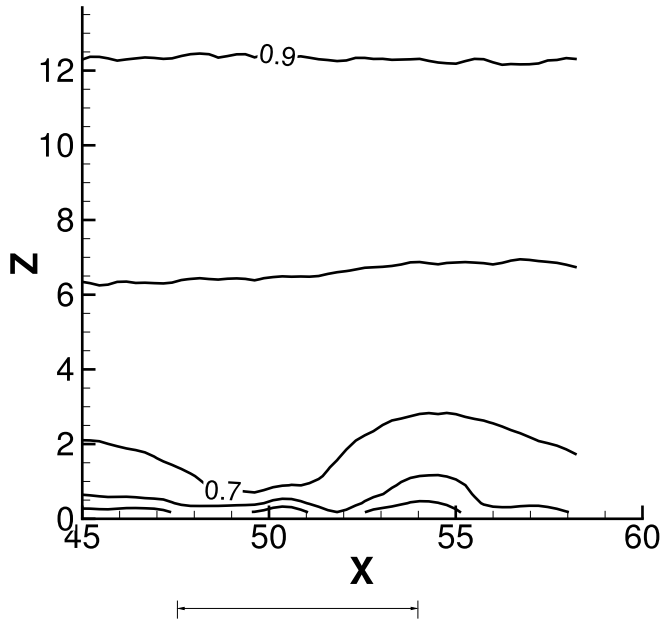

Figure 85: Experimental contours of u-velocity in $y = 0$ center plane at phase = 40° (line below x-axis indicates approximate location of orifice).

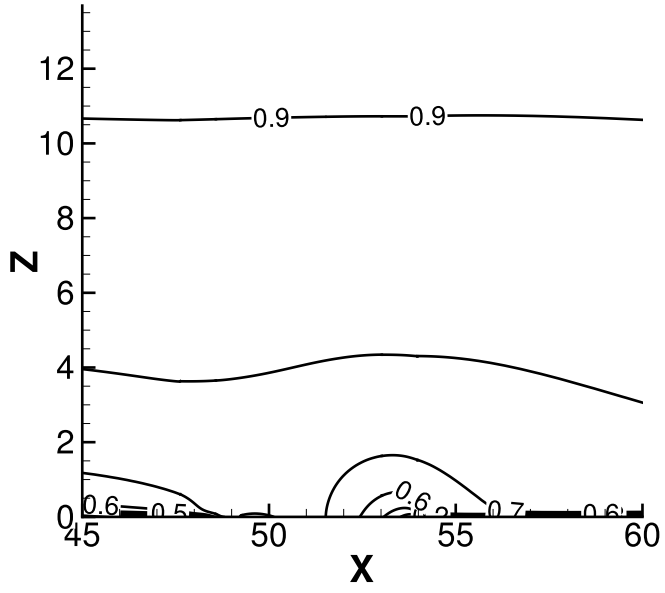

Figure 86: Contours of u-velocity in $y = 0$ center plane at phase = 40°, using SA model on fine grid.

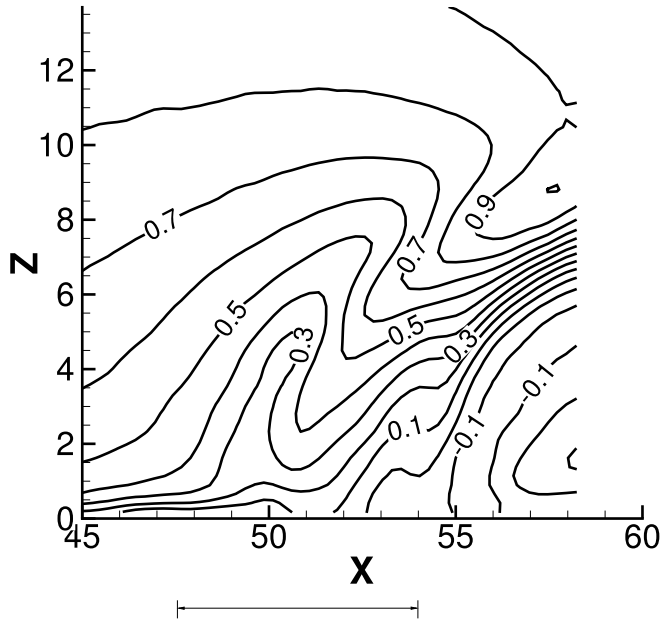

Figure 87: Experimental contours of u-velocity in $y = 0$ center plane at phase = 120° (line below x-axis indicates approximate location of orifice).

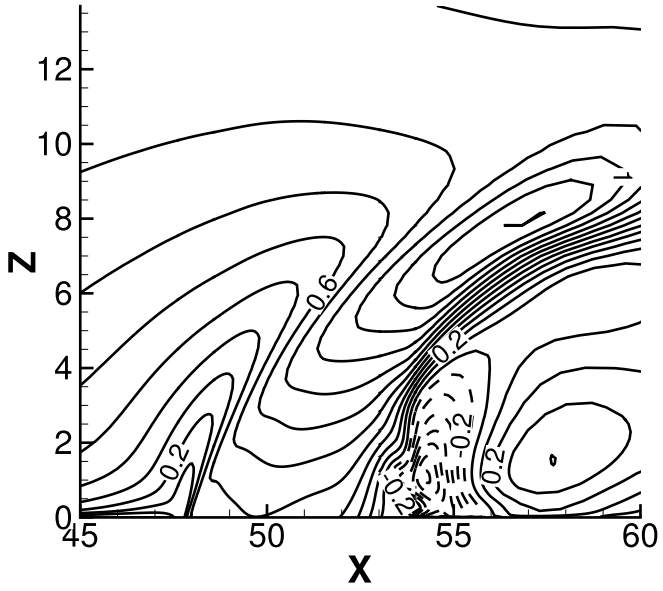

Figure 88: Contours of u-velocity in $y = 0$ center plane at phase = 120°, using SA model on fine grid.

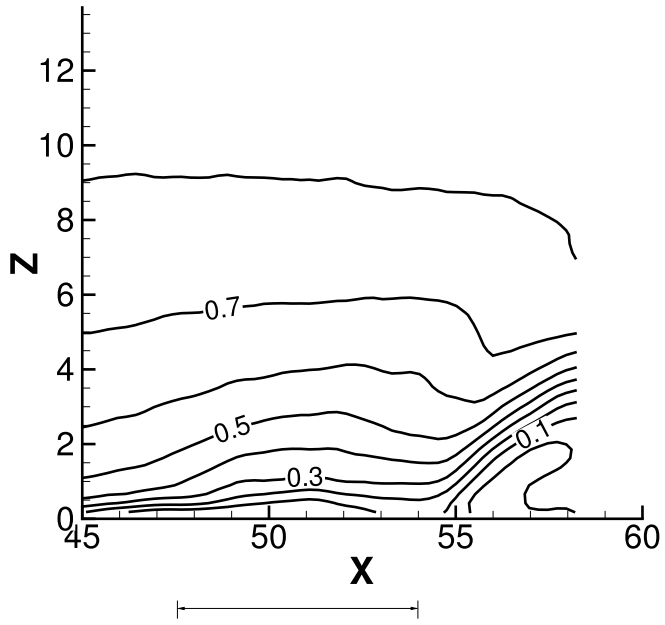

Figure 89: Experimental contours of u-velocity in $y = 0$ center plane at phase = 200° (line below x-axis indicates approximate location of orifice).

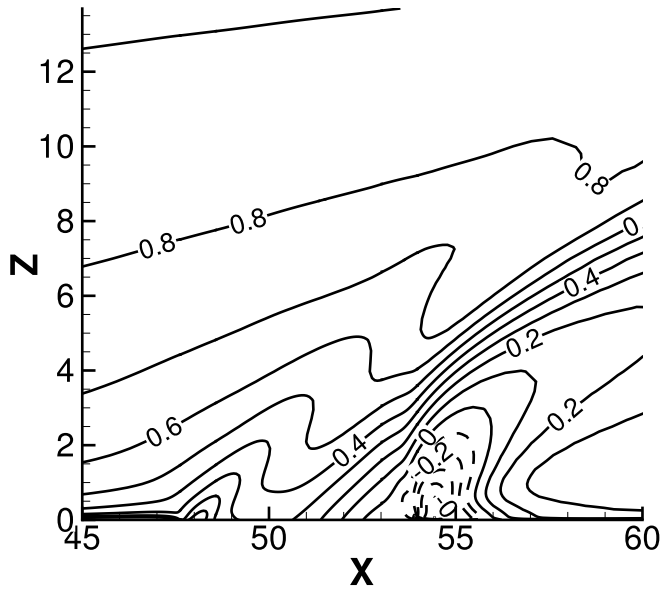

Figure 90: Contours of u-velocity in $y = 0$ center plane at phase = 200°, using SA model on fine grid.

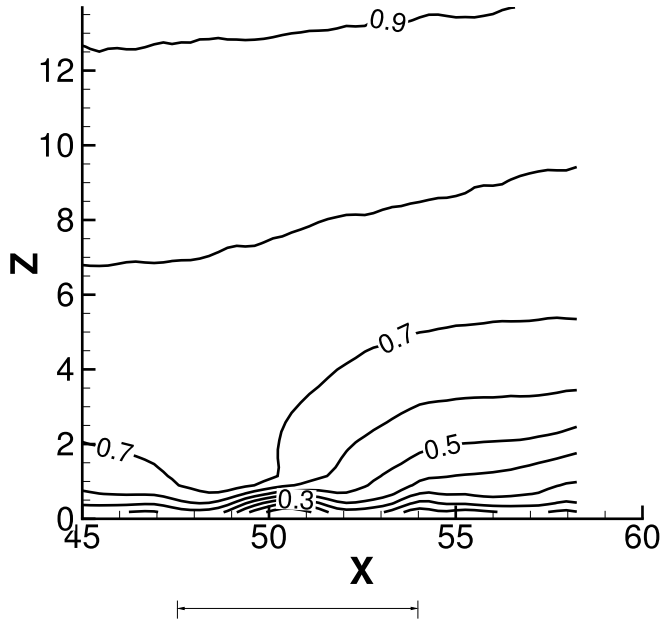

Figure 91: Experimental contours of u-velocity in $y = 0$ center plane at phase = 280° (line below x-axis indicates approximate location of orifice).

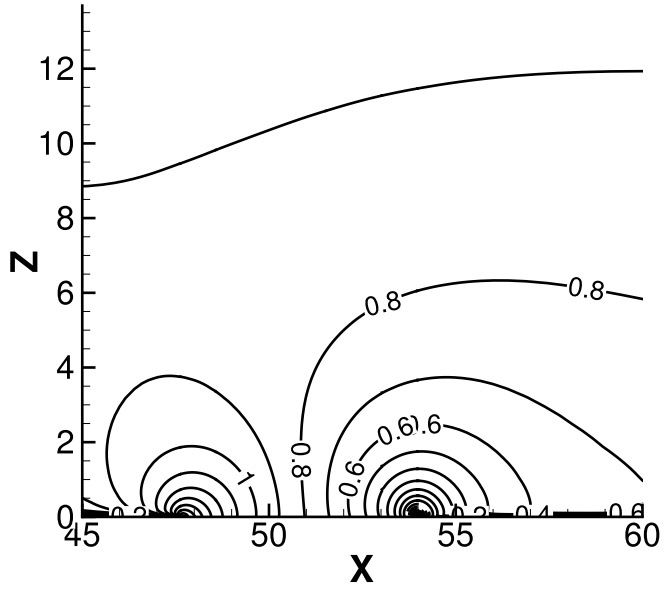

Figure 92: Contours of u-velocity in $y = 0$ center plane at phase = 280°, using SA model on fine grid.

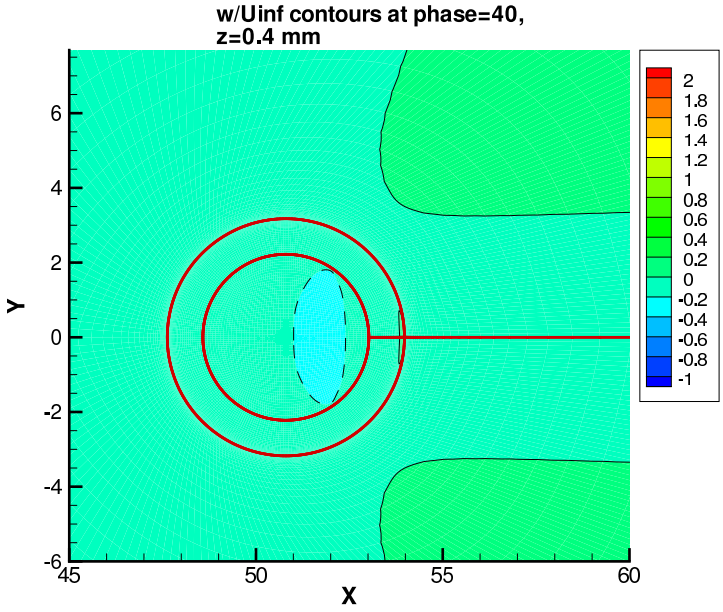

Figure 93: Contours of w-velocity in $z = 0.4$ mm plane over orifice at phase = 40°, using SA model on fine grid (outer circle denotes orifice location).

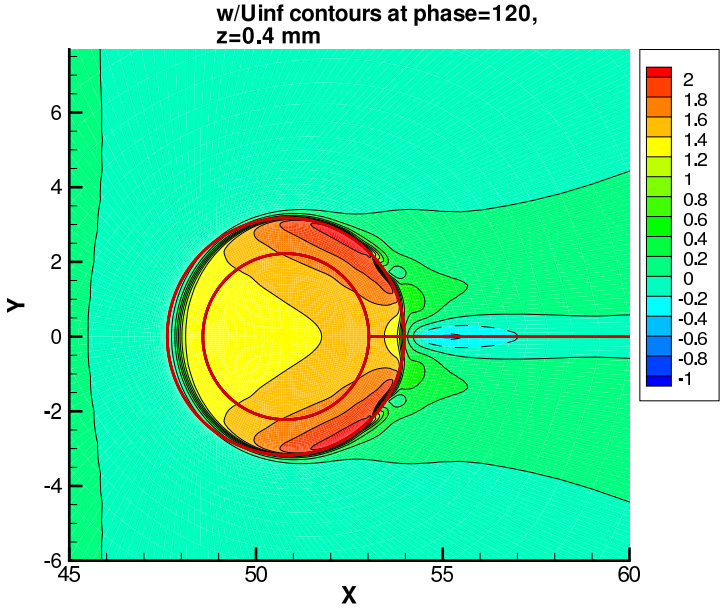

Figure 94: Contours of w-velocity in $z = 0.4$ mm plane over orifice at phase = 120°, using SA model on fine grid (outer circle denotes orifice location).

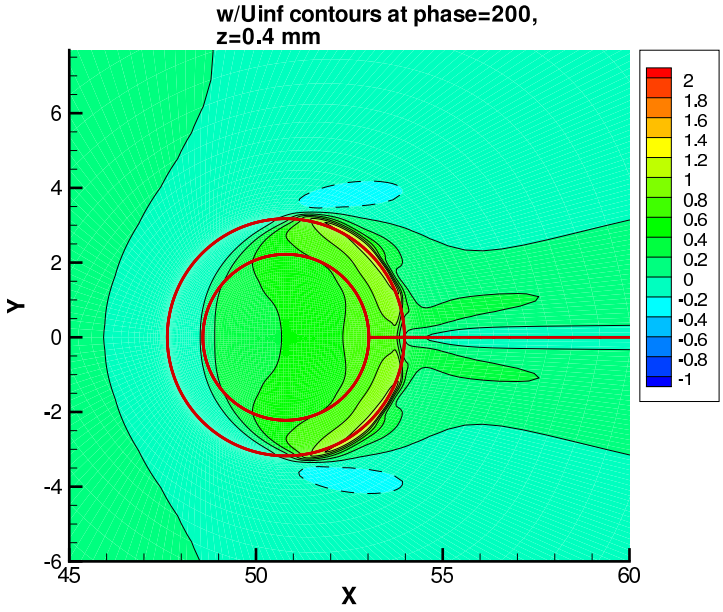

Figure 95: Contours of w-velocity in $z = 0.4$ mm plane over orifice at phase = 200°, using SA model on fine grid (outer circle denotes orifice location).

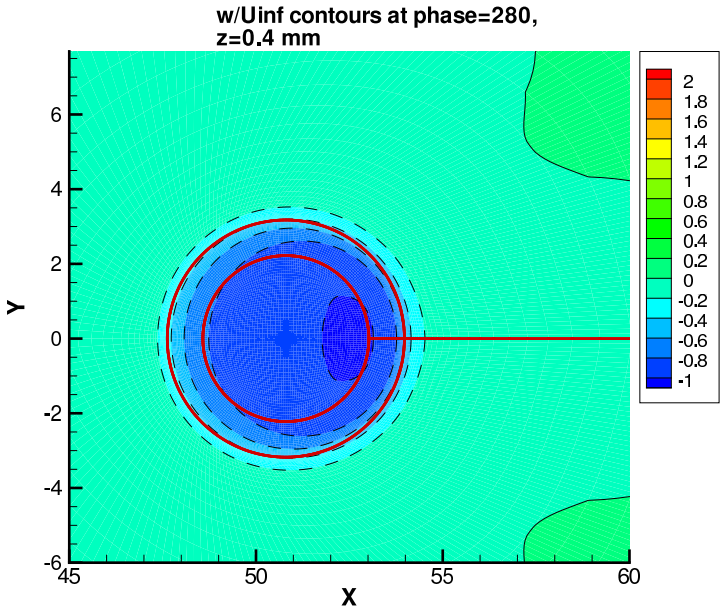

Figure 96: Contours of w-velocity in $z = 0.4$ mm plane over orifice at phase = 280°, using SA model on fine grid (outer circle denotes orifice location).

REPORT DOCUMENTATION PAGE

Form Approved
OMB No. 0704-0188

1. REPORT DATE *(DD-MM-YYYY)*	2. REPORT TYPE	3. DATES COVERED *(From - To)*
01- 10 - 2004	Technical Memorandum	

4. TITLE AND SUBTITLE
Computation of a Synthetic Jet in a Turbulent Cross-Flow Boundary Layer

5a. CONTRACT NUMBER

5b. GRANT NUMBER

5c. PROGRAM ELEMENT NUMBER

6. AUTHOR(S)
Rumsey, Christopher L.

5d. PROJECT NUMBER

5e. TASK NUMBER

5f. WORK UNIT NUMBER
23-762-45-MF

7. PERFORMING ORGANIZATION NAME(S) AND ADDRESS(ES)
NASA Langley Research Center
Hampton, VA 23681-2199

8. PERFORMING ORGANIZATION REPORT NUMBER
L-19052

9. SPONSORING/MONITORING AGENCY NAME(S) AND ADDRESS(ES)
National Aeronautics and Space Administration
Washington, DC 20546-0001

10. SPONSOR/MONITOR'S ACRONYM(S)
NASA

11. SPONSOR/MONITOR'S REPORT NUMBER(S)
NASA/TM-2004-213273

12. DISTRIBUTION/AVAILABILITY STATEMENT
Unclassified - Unlimited
Subject Category 02
Availability: NASA CASI (301) 621-0390 Distribution: Nonstandard

13. SUPPLEMENTARY NOTES
An electronic version can be found at http://techreports.larc.nasa.gov/ltrs/ or http://ntrs.nasa.gov

14. ABSTRACT

A series of unsteady Reynolds-averaged Navier-Stokes computations are performed for the flow of a synthetic jet issuing into a turbulent boundary layer through a circular orifice. This is one of the validation test cases from a synthetic jet validation workshop held in March 2004. Several numerical parameters are investigated, and the effects of three different turbulence models are explored. Both long-time-averaged and time-dependent phase-averaged results are compared to experiment. On the whole, qualitative comparisons of the mean flow quantities are fairly good. There are many differences evident in the quantitative comparisons. The calculations do not exhibit a strong dependence on the type of turbulence model employed.

15. SUBJECT TERMS
Unsteady flow; Synthetic jet; Turbulence model; Validation

16. SECURITY CLASSIFICATION OF:			17. LIMITATION OF ABSTRACT	18. NUMBER OF PAGES	19a. NAME OF RESPONSIBLE PERSON
a. REPORT	b. ABSTRACT	c. THIS PAGE			STI Help Desk (email: help@sti.nasa.gov)
					19b. TELEPHONE NUMBER *(Include area code)*
U	U	U	UU	72	(301) 621-0390